


NEUROPTIMISATION: THE SPIKING WAY TO EVOLVE

PREPRINT

Jorge M. Cruz-Duarte 

University of Lille,
CNRS, Inria, Centrale Lille,
UMR 9189 CRISTAL, F-59000 Lille, France
jorge.cruz-duarte@univ-lille.fr

El-Ghazali Talbi 

University of Lille,
CNRS, Inria, Centrale Lille,
UMR 9189 CRISTAL, F-59000 Lille, France
el-ghazali.talbi@univ-lille.fr

July 14, 2025

ABSTRACT

The increasing energy footprint of artificial intelligence systems urges alternative computational models that are both efficient and scalable. Neuromorphic Computing (NC) addresses this challenge by empowering event-driven algorithms that operate with minimal power requirements through biologically inspired spiking dynamics. We present the *NeuroOptimiser*, a fully spike-based optimisation framework that materialises the neuromorphic-based metaheuristic paradigm through a decentralised NC system. The proposed approach comprises a population of Neuromorphic Heuristic Units (NHUs), each combining spiking neuron dynamics with spike-triggered perturbation heuristics to evolve candidate solutions asynchronously. The *NeuroOptimiser*'s coordination arises through native spiking mechanisms that support activity propagation, local information sharing, and global state updates without external orchestration. We implement this framework on Intel's Lava platform, targeting the Loihi 2 chip, and evaluate it on the noiseless BBOB suite up to 40 dimensions. We deploy several *NeuroOptimisers* using different configurations, mainly considering dynamic systems such as linear and Izhikevich models for spiking neural dynamics, and fixed and Differential Evolution mutation rules for spike-triggered heuristics. Although these configurations are implemented as a proof of concept, we document and outline further extensions and improvements to the framework implementation. Results show that the proposed approach exhibits structured population dynamics, consistent convergence, and milliwatt-level power feasibility. They also position spike-native MHs as a viable path toward real-time, low-energy, and decentralised optimisation.

This work has been submitted to the IEEE Transactions on Evolutionary Computation for possible publication. Copyright may be transferred without notice, after which this version may no longer be accessible.

Keywords Neuromorphic Computing · Event-Driven Asynchronous Optimisation · Neuromorphic Metaheuristics · Spiking Neural Networks · Evolutionary Algorithms.

1 Introduction

Neuromorphic Computing (NC) has emerged as a promising paradigm to address the increasing demands of intelligent systems for low energy consumption, scalability, and real-time responsiveness [1]. This approach, grounded in the biological principles of spiking neural activity, proposes a model of computation based on asynchronous, event-driven processes and collocated memory and processing. Particularly, Spiking Neural Networks (SNNs), as the third generation of neural models, operate with sparse and localised computation, encouraging the implementation of distributed architectures without central synchronisation [2, 3]. These properties are particularly valuable in embedded and edge scenarios, where energy and latency constraints prevail. Platforms such as Loihi, TrueNorth, SpiNNaker, and BrainScaleS represent this shift from synchronous von Neumann architectures to biologically inspired substrates [4]. Hence, SNNs are computationally plausible and hardware-aligned, cobblestoning a new path for sustainable, flexible, and efficient artificial intelligence.

Parallel to this technological advance, heuristic-based algorithms, also known as Metaheuristics (MHs), have proven strong capabilities in addressing complex optimisation problems without requiring gradient information. Evolutionary Algorithms (EAs), Particle Swarm Optimisation (PSO), and Differential Evolution (DE), among others, have provided robust solutions in domains where traditional techniques fail [5, 6]. These methods exploit population-based strategies and adaptive search mechanisms to explore challenging domains. Still, their deployment remains computationally intensive and energy demanding when executed on conventional processors.

The inherent parallelism and locality of most MHs suggest a strong and appealing synergy with NC architectures. These two fields are now mature, and it is only a matter of time before they meet. Thus, the integration of both paradigms will yield a new generation of MHs, whose operators and coordination emerge from spike-based dynamics. Recently, the concept of Neuromorphic-based Metaheuristics (Nheuristics) was introduced as a formal algorithm class that embeds heuristic search mechanisms within spiking neural dynamics [7]. Nheuristics set the foundations for defining a unified design space that covers spiking neuron models, solution encoding, learning mechanisms, and communication topologies.

This work introduces a Neuromorphic Optimiser framework, from now on referred to as *NeuroOptimiser*. This is a general-purpose optimisation framework founded on the Nheuristics paradigm through fully spike-driven computation. The *NeuroOptimiser* architecture consists of multiple Neuromorphic Heuristic Units (NHUs), each embedding heuristic operators within the spike-triggered neuron dynamics. These units evolve candidate solutions asynchronously, embedding heuristic operators within biologically inspired or abstract state transitions. Additionally, we design decentralised coordination mechanisms such as a tensor contraction layer for spike propagation, a neighbour manager for local information exchange, and a high-level selector for global decision-making. We demonstrate the flexibility of the approach by implementing both two-dimensional linear dynamic and Izhikevich (nonlinear) neuron models with multiple spike-triggered rules, including DE-based spike-triggered heuristics. Moreover, we provide an open-source implementation using Intel’s Lava NC framework [8], targeting the Loihi 2 chip, and validate the approach on the BBOB test suite from [9]. Results demonstrate structured search dynamics, consistent convergence behaviour, and sub-watt power estimates under realistic configurations.

2 Related Work

The integration of NC, particularly SNNs, with MH optimisation has rendered notable but fragmentary progress. The existing systems reported primarily target specific combinatorial problems by embedding spiking dynamics within custom architectures, often yielding efficient but rigid solutions.

Several contributions follow this direction. Lin and Fan proposed a transient chaotic neural network based on ferroelectric memristors for the Travelling Salesperson Problem (TSP), achieving improved convergence via polarisation-driven annealing in a handcrafted spiking design [10]. Kim *et al.* presented an NC-based Max-Cut solver using organic memristors, where the architecture’s tight coupling to problem structure yields promising embedded performance [11].

Other approaches have addressed Quadratic Unconstrained Binary Optimisation (QUBO) problems using spike-based computation. Lele *et al.* designed a swarm of spiking solvers for QUBO on RRAM hardware, achieving energy-efficiency operation via compute-in-memory co-design [12]. Similarly, Pierro *et al.* developed a spiking simulated annealing algorithm on Loihi 2, reporting real-time execution and energy savings [13]. Notwithstanding, both implementations remain structurally bound to the QUBO problem class.

Beyond problem-specific designs, several research efforts have studied and explored the broader integration of SNNs and optimisation from a generalisation perspective. Roy *et al.* surveyed SNNs as key components in the development of neuromorphic intelligence, focusing on biologically plausible learning rules, including spike-timing-dependent plasticity, surrogate gradients, and hardware landscape [14]. Withal, their analysis remains within classification and inference tasks, bypassing search and optimisation. Besides, Shen *et al.* reviewed evolutionary spiking neural networks, which utilise evolutionary principles to train deep spiking architectures, often achieving performance comparable to that of conventional methods [15]. Nevertheless, their work centred around neural architectural search without implementing spike-driven heuristics as optimisation operators. Schuman *et al.* introduced the Evolutionary Optimisation for Neuromorphic Systems (EONS) framework, which evolves SNN topology and hyperparameters for deployment on NC simulators [16]. A later variant extended the method to edge computing tasks using hybrid simulation on μ Caspi hardware [17]. While these approaches support hardware-aware adaptation, the evolutionary logic remains CPU-based and offline.

Complementary strategies have explored the application of swarm intelligence in conjunction with spiking-based computation. Fang *et al.* proposed a model integrating SNNs with swarm-based mechanisms for continuous and combinatorial problems, although limited to software simulations sans specific NC hardware alignment [18]. Similarly,

Sasaki and Nakano presented a spiking variant of PSO using deterministic oscillators, delivering theoretical guarantees and competitive performance [19]. However, their model requires manual parameter tuning and lacks hardware implementation. Javanshir *et al.* provided an extensive hardware and algorithmic survey, where evolutionary strategies are acknowledged, including encoding schemes and implementations, but without proposing a spike-based MH framework [20]. More recently, Snyder *et al.* developed a Bayesian optimiser, LavaBO, and related asynchronous coordination extensions within Intel’s Lava NC framework [21–23]. Although the spike activity in these implementations remains a secondary interface, CPU-based Bayesian methods drive the optimisation process.

From these studies, two critical observations emerge. First, there is a decentralised effort to develop energy-efficient MHs by exploiting the architectural affordances of NC substrates. Second, while SNNs are well suited to parallel and low-power execution, existing applications in optimisation remain rigid and problem-specific. The structural compatibility between NC and MH design has yet to yield a general, reusable framework in which both coordination and search arise natively from spike-driven dynamics.

3 Foundations of Neuromorphic Optimisation

This section presents the theoretical foundations of the NeuroOptimiser framework, commencing with core concepts in optimisation and heuristic search, and leading to the formulation of its neuromorphic, spike-driven components.

3.1 Optimisation Problem and Heuristics

The proposed approach is based on the following key concepts, which establish the terms used to describe the approach in the remainder of this section. First of all, we employ the minimisation problem (\mathcal{X}, f, \min) definition such as

$$\mathbf{x}_* = \operatorname{argmin}_{\mathbf{x} \in \mathbb{R}^d} \{f(\mathbf{x})\}, \quad (1)$$

where $\mathbf{x}_* \in \mathcal{X}$ is the optimal solution within the feasible domain $\mathcal{X} \subseteq \mathbb{R}^d$ that minimises the objective function $f : \mathbb{R}^d \mapsto \mathbb{R}$, i.e., $f(\mathbf{x}_*) \leq f(\mathbf{x})$, $\forall \mathbf{x} \in \mathcal{X}$ [24]. This definition inherently incorporates constraints in the feasible domain specification. In contrast,

$$\mathcal{X} = \{\mathbf{x} \in \mathbb{R}^d \mid x_{l,j} \leq x_j \leq x_{u,j}, \forall j \in \mathbb{N}_d\}, \quad (2)$$

stands for a simple, feasible domain, defined by the lower and upper bound constraints $\mathbf{x}_l, \mathbf{x}_u \in \mathbb{R}^d$. In this work, we deal with continuous minimisation problems, but the definition above can be easily extended to other domains.

Now, when addressing optimisation problems using heuristic-based algorithms, particularly those involving multiple probes, it is crucial to consider the concepts of population, neighbourhoods, and the best candidate solution. Therefore, a population \mathbf{X} consists of a finite set of n candidate solutions associated to some units that evolve iteratively over time t , i.e., $\mathbf{X} = \{\mathbf{x}_i\}_{i=1}^n$. Analogously, a neighbourhood is defined as $\mathbf{N} \subseteq \mathbf{X}$. A common structure assumes that each candidate belongs to a neighbourhood of m neighbours, thus $\mathbf{N}_i \subseteq \mathbf{X}$, $\forall i \in \mathbb{N}_n$, with $\#\mathbf{N}_i = m < n$. Another relevant structure considers the historical trajectory of a given candidate, where a neighbourhood consists of its past states such that $\mathbf{N}_i^t = \{\mathbf{x}_i^\tau\}_{\tau=1}^t$. With this, the best candidate solution from a given set is obtained via $\operatorname{argmin}_{\mathbf{x} \in \mathbf{A}} \{f(\mathbf{x})\}$, since \mathbf{A} stands for an arbitrary subset. For instance, we refer to \mathbf{p}_i^t as the particular best candidates in the sets \mathbf{N}_i^t . Plus, employing an auxiliary population $\mathbf{P}^t = \{\mathbf{p}_i^t\}_{i=1}^n$, we determine the global best candidate solution \mathbf{g}^t at time step t , as well as more informed neighbourhoods, i.e., $\mathbf{P}_{n,i}^t \subseteq \mathbf{P}^t$, $\forall i \in \mathbb{N}_n$.

From the perspective of optimisation, these components naturally align with well-established heuristic concepts. A heuristic can be defined as a rule that generates or modifies candidate solutions for a given problem [25, 26]. We follow a layered interpretation that distinguishes between Simple Heuristics (SHs) and Metaheuristics (MHs) based on their operational scope and domain dependency [27]. SHs act directly on the problem domain and can be classified into three categories: generative, perturbative, and selective. Thus, an MH can be presented as,

$$\text{MH} \triangleq \langle h_{\text{init}}, h_{\text{sop}}, h_{\text{fin}} \rangle = h_{\text{fin}}(h_{\text{sop}}) \circ h_{\text{init}}, \quad (3)$$

where h_{sop} is the search operator, which usually comprises a perturbation h_{per} succeeded by a selection h_{sel} of candidates for the next step. The others correspond to the initialisation h_{init} and finalisation h_{fin} heuristics, which are particular implementations of the generative and selective heuristics, respectively. The main difference between h_{sel} and h_{fin} is the working domain, while the former interacts with the problem domain, the latter does it with the heuristic space; i.e., low-level and high-level selectors. Although h_{init} and h_{fin} are crucial for the overall process, h_{sop} is the real signature of the well-known MHs in the literature. For example, consider DE, which has numerous variants in the literature [28]. Most of these variant follow the notation *DE/mutation/differences/crossover* that can be expressed as in (3) using $h_{\text{sop}} = (h_{\text{sel,g}} \circ h_{\text{per,DC}}) \circ (h_{\text{sel,d}} \circ h_{\text{per,DM}})$. This search operator is chiefly composed of a differential mutation

$h_{\text{per,DM}}$ and a differential crossover $h_{\text{per,CR}}$ corresponding to the DE/*mutation/differences*/ and DE/*/crossover* parts. To illustrate these, we selected DE/*current-to-best/1/bin*, such that

$$h_{\text{per,DM}}\{\mathbf{x}_i^t\} \triangleq \mathbf{x}_i^t + F(\mathbf{g}^t - \mathbf{v}_i^t) + F(\mathbf{x}_{r_1}^t - \mathbf{x}_{r_2}^t), \quad (4)$$

$$h_{\text{per,DC}}\{\mathbf{x}_i^t\} \triangleq \mathbf{x}_i^{t+1} \odot \mathcal{H}(p_{\text{CR}} - \mathbf{r}) + \mathbf{x}_i^t \odot \mathcal{H}^c(p_{\text{CR}} - \mathbf{r}), \quad (5)$$

where $F \in [0, 2]$, $r_1, r_2 \sim \mathcal{U}(0, 1)$, $r_1 \neq r_2$, and $\mathbf{r} \ni r_j \sim \mathcal{U}(0, 1)$, and $p_{\text{CR}} \in [0, 1]$. Plus, \odot is the Hadamard-Schur's product, and $\mathcal{H}, \mathcal{H}^c : \mathbb{R}^D \rightarrow \mathbb{Z}_2^D$ are the element-wise Heaviside function and its complement such that $\mathcal{H}(\mathbf{y}) + \mathcal{H}^c(\mathbf{y}) = \mathbf{1}$, for an arbitrary $\mathbf{y} \in \mathbb{R}^d$. Moreover, $h_{\text{sel,d}}$ and $h_{\text{sel,g}}$ stand for the direct and the greedy selection [24].

3.2 Spiking Neuron Models as Adaptive Perturbation Units

Spiking neurons constitute the fundamental computational element in our proposal. They enable dynamic, state-dependent perturbations through biologically grounded membrane potential dynamics [3]. These models simulate the evolution of neuronal states, driven by external inputs and internal synaptic activity, resulting in spike events when the membrane potential exceeds a specific threshold. The Leaky Integrate-and-Fire (LIF) model efficiently captures this behaviour, while more complex models like Izhikevich and Hodgkin–Huxley include ionic channel mechanisms and nonlinear adaptations [2, 29]. We consider the integration of different neuron models to encourage practitioners to implement the most suitable spiking dynamics for their strategies. Thus, each candidate solution \mathbf{x} is represented by d independent spiking neurons that can share information via spike-triggered mechanisms.

First, before describing the particular elements of this model, Figure 1 presents an example of its behaviour on three representative search steps. It features the j^{th} candidate solution component $x_j^t \in \mathfrak{X}_j \subset \mathfrak{X}$ at the step t , corresponding to a neuron, which evolves through spiking-driven state transitions represented with $v_j^t \in \mathfrak{V} \subseteq \mathbb{R}^p$. This is possible due to the transformation $\mathcal{T} : \mathfrak{X}_j \leftrightarrow \mathfrak{V}$, where its corresponding v_j^t updates according to the rules h_d and h_s . This procedure iterates as a new state arises via spike-triggered transition, which fires the spike s_j^{t+1} , within the spiking condition set \mathcal{S} .

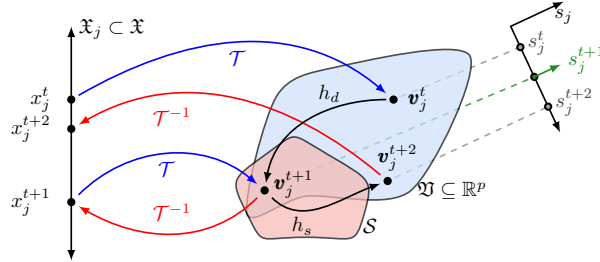


Figure 1: Example of three search steps carried out internally by a spiking neuron in an evolutionary process. A position component x_j^t is mapped via \mathcal{T} to render v_j^t . The blue- and red-shaded regions are the neuromorphic space \mathfrak{V} and the spiking condition set \mathcal{S} , where the dynamic h_d and spike-triggered h_s rules reign. The floating axis s_j shows the associated spiking activity.

We commence dissecting the process overviewed above, focusing solely on the neuromorphic space to establish the foundations of our proposal. A neuron is usually modelled through its membrane potential v^t , which accumulates inputs and evolves dynamically based on synaptic interactions [30]. To describe this behaviour, we regard the LIF model due to its simplicity [2]. It models the neuron's membrane potential charging and discharging dynamics as a leaky capacitor, which is numerically written using the Euler method, such as

$$v^{t+1} \leftarrow \begin{cases} v^t - \frac{\Delta t}{\tau_m} (v^t - v_{\text{rest}} + i_{\text{syn}}^t), & \text{if } v^t < v_{\text{th}}, \\ v_{\text{rest}}, & \text{if } v^t \geq v_{\text{th}}, \end{cases} \quad (6)$$

since τ_m stands for the membrane time constant, v_{rest} corresponds to the resting or equilibrium potential, and i_{syn}^t denotes the synaptic input, and Δt represents the numerical time step [29]. Therefore, when v^t reaches a threshold v_{th} , a spike is fired, triggering an immediate reset. From now on, we assume all variables are nondimensionalised.

This numerical model is low-cost and easy to implement, but it falls short of emulating all the dynamic artefacts of neurons [3]. Notwithstanding, the LIF model sheds some light on how different rules can govern this internal dynamic, and how problems might require specific configurations for threshold, state-update dynamics, and spike-triggering conditions.

Moving forward with a richer-behaviour model, we regard the Izhikevich model, which is also computationally efficient and capable of reproducing the spiking and bursting artefacts of some kinds of neurons [29]. This model comprises two differential equations that, similar to LIF, can be expressed in their numerical form as follows

$$\begin{pmatrix} v^{t+1} \\ u^{t+1} \end{pmatrix} \leftarrow \begin{cases} h_d(v^t, u^t), & \text{if } v^t < v_{\text{th}}, \\ h_s(v^t, u^t), & \text{if } v^t \geq v_{\text{th}}, \end{cases} \quad (7)$$

with

$$\begin{aligned} h_d \begin{pmatrix} v^t \\ u^t \end{pmatrix} &\triangleq \begin{pmatrix} v^t + (\frac{1}{25}(v^t)^2 + 5v^t + 140 - u^t + i_{\text{syn}}^t)\Delta t \\ u^t + a(bv^t - u^t)\Delta t \end{pmatrix}, \\ h_s \begin{pmatrix} v^t \\ u^t \end{pmatrix} &\triangleq \begin{pmatrix} c \\ u^t + d \end{pmatrix}. \end{aligned} \quad (8)$$

Likewise, v^t , v_{th} , and i_{syn}^t stand for the membrane potential, threshold potential, and input current. In addition, u^t corresponds to the recovery variable, and a , b , c , and d are control parameters [31].

With these expressions, it is time to define the dynamical updating rule h_d and the spike-triggered rule h_s , i.e., $h_d, h_s : \mathbb{R}^p \mapsto \mathbb{R}^p$. The former accounts for the neuron's intrinsic dynamics, and the latter models the after-spike reset behaviour. Now, we specify the internal neuromorphic state vector, such as $\mathbf{v}_j \in \mathfrak{V} \subseteq \mathbb{R}^p$, where $p \geq 1$ is given by the spiking neuron model, evolving under a defined dynamic. In this state, $v_{1,j} \in \mathbf{v}_j$ acts as an analogue to membrane potential, while $v_{k,j}$, $\forall k \in \mathbb{N}_p \setminus \{1\}$, are model-specific auxiliary components.

Therefore, we propose a generalised neuron model that applies perturbations within a transformed space, where rules or heuristics are dynamically adjusted based on spike-triggered updates. The state variable change is given by,

$$\mathbf{v}^{t+1} \leftarrow \begin{cases} h_d(\mathbf{v}_j^t), & \text{if } \Phi(\mathbf{v}_j^t, t, \dots) \neq 1, \\ h_s(\mathbf{v}_j^t), & \text{otherwise,} \end{cases} \quad (9)$$

where

$$\Phi(\mathbf{v}_j^t, t, \dots) \triangleq \bigvee_k \varphi_k(\mathbf{v}_j^t, t, \dots), \quad (10)$$

since $\Phi(\mathbf{v}_j^t, t, \dots) : \mathfrak{V} \times \mathbb{Z}_+ \times \dots \mapsto \mathbb{Z}_2$ corresponds to the spiking condition function depending on either the state variable or external information. In this work, we consider two main spiking conditions to determine Φ for simplicity. The first $\varphi_s(\mathbf{v}_j^t)$ is directly related to the spiking condition set \mathcal{S} , which could be part, at least partially, of \mathfrak{V} , as Figure 1 depicts. Hence, we can recursively specify that $\mathcal{S} = \{\mathbf{v}_j \in \mathfrak{V} \mid \varphi_s(\mathbf{v}_j) = 1\}$. The simplest φ_s implementation stands for the thresholding described for the LIF and Izhikevich models, i.e.,

$$\varphi_s(\mathbf{v}_j) = |v_{1,j}| \geq \vartheta_j, \quad (11)$$

where $\vartheta_j \in \mathbb{R}_+$ is a threshold membrane potential.

Associated with the \mathbf{v}_j changes, the spiking signal $s_j \in \mathbb{Z}_2$ represents the self-firing events that a neuron produces. Thus, the function φ_s can also be employed as an indicator function, such that the s_j generation can be defined as,

$$s_j^t \leftarrow \varphi_s(\mathbf{v}_j^t). \quad (12)$$

This firing event is complemented by presynaptic signals from neighbouring units, whose activity is mediated by the spike-driven communication mechanism established in the SNN.

Additionally, the second condition, $\varphi_a(\mathbf{v}_j^t)$, corresponds to spikes induced by the environment, typically described as an activation signal $a_j \in \mathbb{Z}_2$ determined from spikes fired in the neighbourhood. This indicates whether adjacent neurons have recently emitted action potentials. Hence, the simplest definition for this function stands for $\varphi_a(\mathbf{v}_j^t, \dots) = a_j^t$.

Let us now instantiate the illustrative example in Figure 1 with concrete data. The dynamic behaviour of spiking neurons is best understood through their phase portraits, where, for two-dimensional models, one can directly observe the evolution of the membrane potential and the recovery variable under diverse regimes. In this context, we implement the Izhikevich model using (9) with h_d and h_s as defined in (8), and a spiking condition Φ and region \mathcal{S} determined by φ_s in (11), setting $\vartheta_j = 30$. For the simulation, we use $\Delta t = 0.01$ and $T = 100$.

Figure 2 depicts the phase-space trajectories and their associated signals of several cortical, resonator, and thalamo-cortical neurons, generated with the Izhikevich model and using the parameters reported in [31]. The corresponding time series of the membrane potential, the recovery variable, and the spike signal accompany each portrait. From a dynamic systems perspective, h_d governs the evolution of \mathbf{v} , capturing the neuron's intrinsic dynamics. This corresponds to the trajectories observed following the vector field before reaching the spiking threshold. Once a spike occurs, the

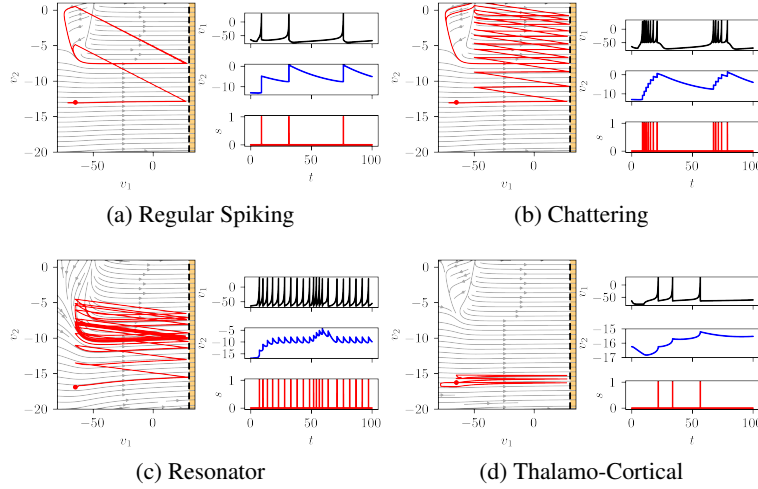


Figure 2: Phase portraits (v_1 vs. v_2) and time signals (v_1, v_2, s vs. t) of the four dynamical behaviours generated using the Izhikevich model and the parameters described in [31]. The dashed black line and orangish-shaded region represent the thresholding condition φ_s and spiking region \mathcal{S} .

system experiences an instantaneous reset through h_s , as indicated by the abrupt jumps where trajectories are reset to new states.

To wrap up the idea mentioned above, let us consider a simpler model based on a two-dimensional dynamic system for a linear deterministic behaviour under h_d and stochastic spiking dynamics under h_s , as shown below

$$\begin{aligned} h_d(\mathbf{v}) &\triangleq \mathbf{v} + \mathbf{A}\mathbf{v}\Delta t, \\ h_s(\mathbf{v}) &\triangleq \vartheta_1 + \vartheta_2 r_1 e^{i2\pi r_2}, \quad r_1, r_2 \sim \mathcal{U}(0, 1). \end{aligned} \quad (13)$$

For this example, we choose a neuromorphic space $\mathfrak{V} = [-2, 2]^2$ and a disc-shaped spiking subset \mathcal{S} defined through,

$$\varphi_s(\mathbf{v}) = \begin{cases} \|\mathbf{v}\|_2 \leq \vartheta_{\text{attractor}}, & \text{if } \text{tr}(\mathbf{A}) \leq 0, \\ \|\mathbf{v}\|_2 \geq \vartheta_{\text{repeller}}, & \text{if } \text{tr}(\mathbf{A}) > 0, \end{cases} \quad (14)$$

where $\vartheta_{\text{attractor}} = 0.5$ and $\vartheta_{\text{repeller}} = 1.5$ are thresholds for stable and unstable equilibrium points. Respectively, the pair $(\vartheta_1, \vartheta_2)$ for h_s are chosen $(0.5, 1.0)$ and $(0.0, 1.5)$. We select these cases to exemplify how we can utilise the system's nature to design spiking cores by adapting thresholding mechanisms to the process of evolution. Plus, the linear coefficients of h_d and initial points were selected to display the state evolution under four different equilibrium points according to [32]. For the simulation, we employ $\Delta t = 0.01$ and $T = 20$.

Similar to the previous portraits, Figure 3 shows the phase-space trajectories and time signals for four illustrative systems. In this case, two trajectories (red and blue lines) per class start from a marked red point, but only the blue one changes when it enters the orangish-shaded region representing the spiking condition set. The first and second rows of Figure 3 correspond to stable and unstable behaviours. Moreover, the first column depicts fast dynamics, i.e., while trajectories in the stable node converge to the equilibrium, φ_s prevents them from reaching it, in the unstable case, trajectories diverge but are bounced back. The second column portrays spiral behaviours with slower evolution due to complex eigenvalues.

3.3 Heuristic Interpretation of Spiking Dynamics

Figure 2 and 3 support the importance of state-dependent changes in shaping the behaviour of neuromorphic optimisation strategies. This formulation opens a pathway for integrating heuristic operations as rules that modify candidate solutions through spike-driven state transitions. So, designing such a spiking neuron requires specifying three principal components according to (9): the dynamic update rule h_d , the spiking condition function Φ to control \mathcal{S} , and the spike-triggered rule h_s . These components, which can be considered heuristics, must be carefully defined to shape the search dynamics, including the spiking conditions, which themselves act as selection criteria. In the following paragraphs, we describe these components from a heuristic perspective.

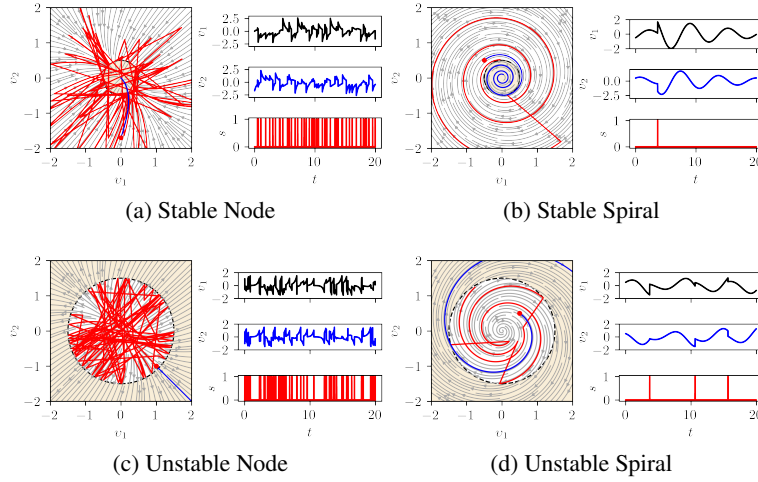


Figure 3: Phase portraits (v_1 vs. v_2) and time signals (v_1, v_2, s vs. t) of four equilibrium points in a linear system. The dashed black circle and orangish-shaded region depict the thresholding condition φ_s and spiking region \mathcal{S} . The red and blue lines show trajectories with and without spiking, respectively.

Foremost, spikes are fired when the neuron’s internal state satisfies a condition φ_s , which acts as a selection predicate for triggering transitions. The simplest case corresponds to the thresholding heuristic defined in (11). Still, this principle can be extended to incorporate additional parameters reflecting internal dynamics or contextual information from the optimisation process. Some other representative conditions can be,

$$\varphi_s(\mathbf{v}_j, \dots) \triangleq \|\hat{\boldsymbol{\alpha}}_{\text{spk}} \cdot \mathbf{v}_j\|_q > \vartheta_j, \quad (15a)$$

$$\varphi_s(\mathbf{v}_j, \dots) \triangleq \|\mathbf{v}_j\|_2 < \varepsilon_{\text{spk}}/(1+t). \quad (15b)$$

From these, the weighted Minkowski (ℓ_q -norm) condition in (15a) extends (11), using the unit vector $\hat{\boldsymbol{\alpha}}_{\text{spk}} \in [0, 1]^p$ to modulate each component’s relevance. Plus, the condition in (15b) implements a proximity criterion to the origin with a shrinking tolerance $\varepsilon_{\text{spk}} > 0$, useful for systems with stable equilibrium points, e.g., Figure 3a and 3b.

Most of the parameters in (15) are either constants, deterministic sequences, or random variables. While the threshold ϑ_j can be defined as a scalar, this static choice may ignore the potential for environment-aware modulation of spiking activity during the search process. To introduce flexibility and contextual awareness, we consider the following variants,

$$\vartheta_j \triangleq \alpha_{\text{thr}}, \quad (16a)$$

$$\vartheta_j \triangleq \alpha_{\text{thr}}|g_j - p_j|, \quad (16b)$$

$$\vartheta_j \triangleq \alpha_{\text{thr}}|x_{\text{ref},j} - p_j|. \quad (16c)$$

From these, $\alpha_{\text{thr}} > 0$ is the base value that directly defines the threshold in the fixed case at (16a). The difference-based variant in (16b), inspired by [19], uses the distance between the global $p_j \in \mathbf{p}$ and particular $g_j \in \mathbf{g}$ best components, whereas (16c) employs a target reference $x_{\text{ref},j} \in \mathbf{x}_{\text{ref}}$ instead of the global best component.

Subsequently, the heuristic h_d is defined by the evolution of a dynamic system chosen for modelling the spiking neuron. When the system implemented is discrete, this expression can be used directly. For example, two-dimensional strange attractors such as the Lozi and Hénon maps [32, 33]. When the system is continuous, with the form given by $\dot{\mathbf{v}}_j = \mathbf{g}(\mathbf{v}_j)$, we must consider a numerical integration method for approximating the new state \mathbf{v}_j^{t+1} . The simplest approximation method, such as the Euler method [32], is given by,

$$h_d(\mathbf{v}_j) \triangleq \mathbf{v}_j + \mathbf{g}(\mathbf{v}_j)\Delta t, \quad (17)$$

where the time step $\Delta t > 0$ must be specified and can be considered to control the detail level during the dynamic search around \mathcal{V} . Two examples of these systems are discussed above, which are already in their numerical form in (8) and (13). We avoid presenting them in their differential expression for brevity. Still, their corresponding \mathbf{g} forms are straightforward to infer from (8) and (13), using (17). Notice that we focus on two-dimensional systems, but systems with one or more than two dimensions can also be implemented with ease, e.g., LIF, Lorenz, and Hodgkin-Huxley [32, 34]. Naturally, other alternative numerical methods can be considered, e.g., the 4th-order Runge-Kutta algorithm [32].

Upon spiking, the spike-triggered heuristic h_s performs a transition over the internal state according to a perturbative operation. According to Section 3.1, this rule can be formalised as $\mathbf{v}_j^{t+1} \leftarrow h_s(\mathbf{v}_j^t) \triangleq h_{\text{per}}\{\mathbf{v}_j^t\}$, where h_{per} is chosen from a finite but massive set of heuristic operators existing in the literature. We consider four representative classes of perturbative rules, all of which are consistent with the original reset strategies from spiking neuron models [3] and the definition of simple heuristics [27].

The first class corresponds to a stochastic reset, related to a random search operation, defined as

$$h_s(\mathbf{v}_j^t) \triangleq \boldsymbol{\xi}_j^t \quad (18)$$

since the state is sampled from the neuromorphic space \mathcal{U} using any random distribution, e.g., $\boldsymbol{\xi}_j^t \ni \xi_{j,k}^t \sim \mathcal{N}(0, 1)$.

Subsequently, the second class represents a reset toward a well-known state, similar to the reset mechanism of the LIF and Izhikevich models [2]. We use the best visited state $\bar{\mathbf{v}}_j^t = \mathcal{T}\{p_j^t\}$, perturbed with slight noise $\boldsymbol{\epsilon}_j^t \ni \epsilon_{j,k}^t \sim \mathcal{N}(0, \sigma)$ to avoid hitting the exact position, such as,

$$h_s(\mathbf{v}_j^t) \triangleq \bar{\mathbf{v}}_j^t + \boldsymbol{\epsilon}_j^t, \quad (19)$$

where $\sigma > 0$ corresponds to the standard deviation of the component-wise noise applied to $\bar{\mathbf{v}}_j^t$.

The third class defines a directional displacement from the current state toward a given good-quality state $\mathbf{v}_{\text{ref}}^t$, as shown

$$h_s(\mathbf{v}_j^t) \triangleq \mathbf{v}_j^t + \alpha_d(\mathbf{v}_{\text{ref}}^t - \mathbf{v}_j^t) + \boldsymbol{\epsilon}_j^t, \quad (20)$$

since $\mathbf{v}_{\text{ref}}^t$ can be the neuromorphic space representation via \mathcal{T} of either the particular best position, the global best position or a combination of both. Plus, $\alpha_d > 0$ controls the step size and $\boldsymbol{\epsilon}_j^t$ introduces stochastic variability.

Lastly, the fourth class of spike-triggered heuristics is based on mutation strategies from DE [28], which corresponds to the next step of the generalisation path previously described. Therefore, based on the perturbation heuristic in (4) for the DE/*current-to-best*/1 mutation, we rewrite this and include another in terms of the state variables, such as

$$h_s(\mathbf{v}_j^t) \triangleq \mathbf{v}_j^t + F(\bar{\mathbf{v}}_j^t - \mathbf{v}_j^t) + F(\bar{\mathbf{v}}_{r_1,j}^t - \bar{\mathbf{v}}_{r_2,j}^t), \quad (21a)$$

$$h_s(\mathbf{v}_j^t) \triangleq \mathbf{v}_j^t + F(\bar{\mathbf{v}}_{r_1,j}^t - \mathbf{v}_j^t) + F(\bar{\mathbf{v}}_{r_2,j}^t - \bar{\mathbf{v}}_{r_3,j}^t), \quad (21b)$$

These correspond to the *current-to-best*, *rand-to-best*, and *current-to-rand*, respectively. Regard that $\bar{\mathbf{v}}_{r_k}^t$ are distinct state vectors randomly sampled and transformed from $\mathbf{P}_{n,i}^t$, and $\bar{\mathbf{v}}_j^t$ denote the global best state representation using \mathcal{T} .

3.4 Bidirectional Mapping

The mapping between candidate positions and the neuromorphic space is crucial for implementing the proposed framework. A bidirectional transformation \mathcal{T} , as shown in Figure 1, is hence required to relate the neuromorphic and problem spaces. Therefore, the \mathcal{T} between x_j and \mathbf{v}_j can be defined as $\mathfrak{V} \ni \mathbf{v}_j \triangleq \mathcal{T}\{x_j\} \iff \mathcal{T}^{-1}\{x_j\} \triangleq x_j \in \mathfrak{X}$. A simple implementation of \mathcal{T} corresponds to the linear mapping,

$$\mathbf{v}_j = \mathcal{T}(x_j) \triangleq (\alpha(x_j - x_{\text{ref},j}), \quad 2r - (1 - x_{\text{ref},j}))^\top, \quad (22)$$

where $\alpha \in \mathbb{R}$ is a gain factor, $x_{\text{ref},j} \in \mathbf{x}_{\text{ref}} \in \mathfrak{X}$ is a reference point, and $r \sim \mathcal{U}(0, 1)$ is a random value. Notice that the first component is directly related to the candidate position element, while the second component introduces a stochastic perturbation into the encoding process. This random value must be retained throughout execution to ensure deterministic reversibility and consistent internal dynamics.

On the one hand, α controls the encoding resolution because this factor scales the displacement from \mathbf{x}_{ref} . Thus, small α values promote smoother dynamics, whereas larger ones amplify sensitivity to positional deviations. For that reason, choosing α correctly, depending on the problem's nature, boosts a rich and detailed search. The most straightforward setup can be $\alpha = 1$, which works for most cases but should be considered for fine-tuning tasks. On the other hand, \mathbf{x}_{ref} opens a colourful palette of search behaviours across the problem domain, including focused local refinement, exploratory displacement, and collective coordination through neighbourhood-informed centring. Similar to the previous essential components, we consider distinct references, for example,

$$\mathbf{x}_{\text{ref}} \triangleq w_1 \mathbf{p} + w_2 \mathbf{g}, \quad (23a)$$

$$\mathbf{x}_{\text{ref}} \triangleq w_1 \mathbf{p} + w_2 \mathbf{g} + \sum_{k=1}^m w_{k+2} \mathbf{p}_k, \quad (23b)$$

where p_k denotes the k^{th} neighbour's best-known position, m is the number of neighbours, and $\{w_k\}_{k=1}^m$ is a set of normalised weights. For simplicity, we adopt uniform weighting, ensuring even contribution and preserving neutrality across influence sources [19]. Nevertheless, weighted reference models based on additional information, such as fitness values, can be considered a promising research avenue.

4 The Neuromorphic Optimisation Framework

4.1 Overall Architecture of NeurOptimiser

Figure 4 depicts the general structure of the NeurOptimiser, which requires essential parameters before starting the procedure, such as the problem (\mathcal{X}, f, \min) , the number of Neuromorphic Heuristic Units (NHUs) n , and the adjacency matrices $W_s, W_x \in \mathbb{Z}_2^{n \times n}$ for the SNN and information neighbourhoods. The NeurOptimiser is composed of n NHUs that process and refine candidate solutions. Plus, it comprises a Tensor Contraction Layer, a Neighbour Manager, and a High-Level Selector, which coordinate the transmission and reception of essential encoded information, such as spikes, candidate positions, and fitness values. These components are conceived as asynchronous processes using Intel's Lava NC framework, targeting the Loihi 2 chip [8].

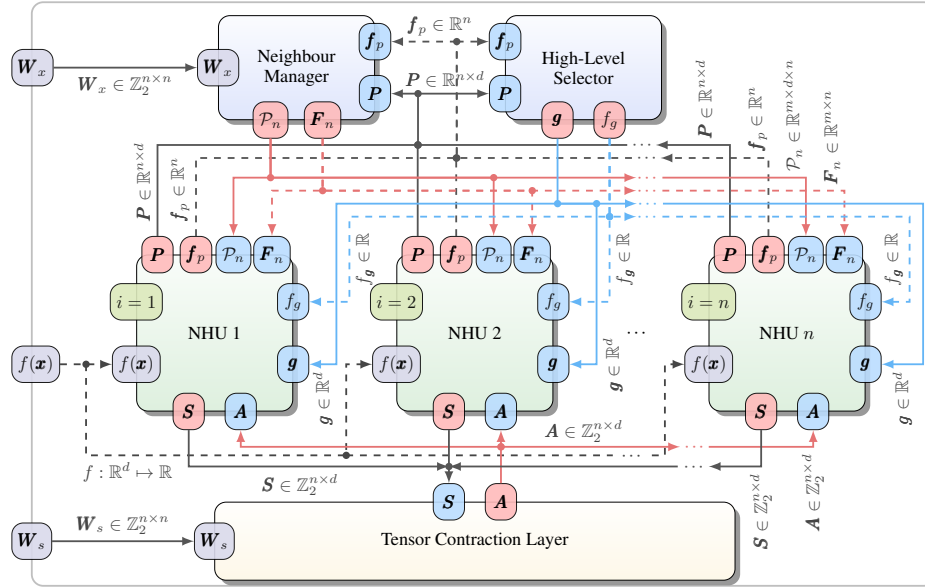


Figure 4: Neuromorphic Optimiser (NeurOptimiser) architecture composed of n Neuromorphic Heuristic Units (NHUs) units, a Tensor Contraction Layer, a Neighbourhood Manager, and a High-Level Selector.

As an overview, the neurOptimiser's process is described as follows. First, NHUs produce their initial candidate solution, while other processes wait until they have information in their respective input ports. After several steps, we can summarise the asynchronous behaviour of each process, such as:

- A NHU reads all its communication channels to process the information independently and then updates its current position and spiking signal.
- The Tensor Contraction Layer receives every spiking signal from NHUs, processes them in a matrix structure, and then propagates the resulting activations to all NHUs.
- The Neighbour Manager reads the particular positions and their fitness from NHUs, processes them, and shares the information grouped by neighbourhoods.
- The High-Level Selector receives the same information that the Neighbour Manager receives and selects the best candidate position. It then broadcasts this to all NHUs.

Each process is detailed in this section's remaining paragraphs.

4.2 Internal Structure of a Neuromorphic Heuristic Unit

NHUs are designed as self-contained modules responsible for encoding, evaluating, and updating candidate solutions during the optimisation process. Figure 5 shows the NHU’s internal architecture comprising two main processes, i.e., Spiking Core and Selector. Besides, it also utilises three information management components serving as I/O peripherals, i.e., a Spiking Handler, a Receiver, and a Sender. These internal processes are briefly described as follows:

- The Spiking Core encodes and modifies candidate solutions using d spiking neurons.
- The Selector evaluates a given position using the objective function f , and maintains the local solution (\mathbf{p}, f_p) depending on the selection criterion.
- The Spiking Handler manages spiking communication by encoding local spike events into the global matrix \mathbf{S} and decoding activation patterns \mathbf{A} .
- The Sender broadcasts the local information to the network by encoding (\mathbf{p}, f_p) into shared structures $(\mathbf{P}, \mathbf{f}_p)$.
- The Receiver gathers information from neighbours and extracts relevant data $(\mathbf{P}_n, \mathbf{f}_n)$ for local usage.

Moreover, the position index i (encoded in the `agent_id`) is only shared with those processes interacting with external information. Likewise, the objective function is only accessed by the Selector. The subsequent paragraphs of this subsection detail these internal processes.

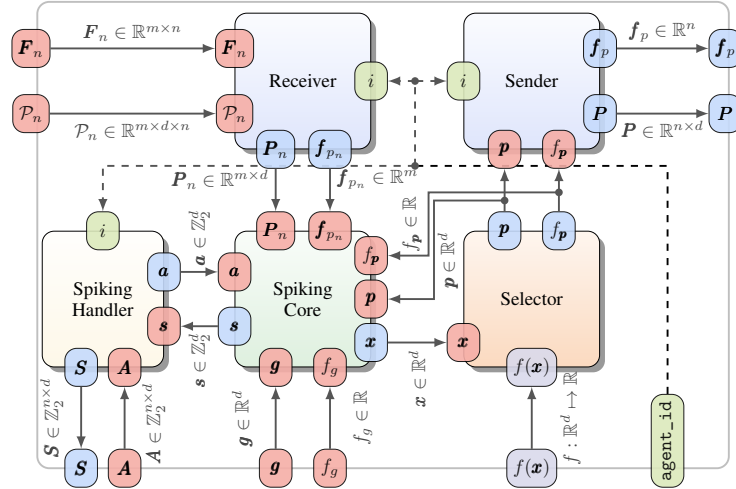


Figure 5: Neuromorphic Heuristic Unit (NHU) architecture comprising two main processes, Spiking Core and Selector; and three auxiliary processes, Spiking Handler, Receiver, and Sender, for receiving and sending information.

4.2.1 Spiking Core

This process is the central component of the NHU. It comprises d spiking neurons that encode \mathbf{x} and define the substance of our approach. To implement this process, the key components required include the transformation \mathcal{T} , the spiking condition function Φ , and the dynamic updating h_d and spike-triggered h_s heuristics. Algorithm 1 details this asynchronous process, which can be summarised in three main blocks. The first one (lines 1-3) corresponds to the initialisation for preparing and sending the first candidate solution. The second (lines 4-6) stands for waiting and reading the relevant information from ports. Once information is available, the third block (7-14) performs the heuristic-based neuromorphic procedure detailed in Section 3.

4.2.2 Selector

This process evaluates a candidate solution \mathbf{x} using f and updates the local reference \mathbf{p}, f_p throughout the evolutionary process. Algorithm 2 presents its internal process, although simple, it implements a key mechanism in the behaviour of the NHU, mainly because the objective function evaluation may involve high computational cost, delayed response, black-box conditions, and surrogate implementations in practical applications [35]. This process employs a greedy selection strategy, which is crucial for ensuring the propagation of high-quality solutions throughout the search process.

Algorithm 1: Spiking Core asynchronous process.

InPorts: $\mathbf{a}, \mathbf{p}, \mathbf{g}, \mathbf{P}_n, f_g, f_p, \mathbf{f}_{p_n}$ ▷ Activation, positions, and fitness
OutPorts: \mathbf{s}, \mathbf{x} ▷ Spiking signal and candidate solution

```

1:  $\mathbf{x}, \mathbf{p}, \mathbf{g}, f_p, f_g, \mathbf{P}_n, \mathbf{f}_{p_n} \leftarrow \text{INITIALISE}()$ 
2:  $\mathbf{a}, \mathbf{s} \leftarrow \text{INITIALISEWITH}(\mathbf{0}_d)$ 
3:  $\text{SEND}(\mathbf{s}, \mathbf{x})$ 
4: while  $\text{RUNCONDITION}()$  do ▷ Asynchronous execution
5:    $\text{WAITFORINPUTS}()$  ▷ Asynchronous event handling
6:    $\mathbf{a}, \mathbf{g}, \mathbf{p}, f_g, f_p, \mathbf{P}_n, \mathbf{f}_{p_n} \leftarrow \text{RECEIVE}()$ 
7:   for each  $j \in \mathbb{N}_d$  do
8:      $\mathbf{v}_j \leftarrow \mathcal{T}(x_j)$  ▷ Transform position to state
9:      $s_j \leftarrow \varphi_s(\mathbf{v}_j)$  ▷ Determine self-spiking condition
10:    if  $\Phi(\mathbf{v}_j, \dots)$  then ▷ Spiking condition function
11:       $\mathbf{v}_j \leftarrow h_s(\mathbf{v}_j)$  ▷ Apply spike-transition rule
12:    else
13:       $\mathbf{v}_j \leftarrow h_d(\mathbf{v}_j)$  ▷ Apply dynamical rule
14:       $x_j \leftarrow \mathcal{T}^{-1}(\mathbf{v}_j)$  ▷ Transform state back to position
15:   $\text{SEND}(\mathbf{s}, \mathbf{x})$ 

```

Algorithm 2: Selector asynchronous process.

InPorts: \mathbf{x} ▷ Candidate position
OutPorts: \mathbf{p}, f_p ▷ Best known position and its fitness

```

1: while  $\text{RUNCONDITION}()$  do ▷ Asynchronous execution
2:    $\text{WAITFORINPUTS}()$  ▷ Asynchronous event handling
3:    $\mathbf{x} \leftarrow \text{RECEIVE}()$ 
4:    $f_x \leftarrow f(\mathbf{x})$  ▷ Evaluate the candidate solution
5:   if  $f_x < f_p$  or  $\neg \text{is\_init}$  then ▷ Greedy selection
6:      $\mathbf{p} \leftarrow \mathbf{x}, f_p \leftarrow f_x$ 
7:      $\text{is\_init} \leftarrow \text{True}$ 
8:    $\text{SEND}(\mathbf{p}, f_p)$ 

```

4.2.3 Spiking Handler

This process plays a critical role as a communication interface, linking each NHU to the collective spike-driven dynamics of the SNN, despite spiking neurons being unaware of this global structure from a local perspective. This biologically inspired process emulates the presynaptic function of neurons by receiving information from neighbours and interpreting it as activation events. Algorithm 3 details the procedure of this component that, contrary to those presented above, additional information about the NHU identity (index i) is needed for proper encoding and decoding. Specifically, the handler receives a spike vector \mathbf{s} from the core and an activation matrix \mathbf{A} from the SNN, updates the corresponding row of the global spike matrix \mathbf{S} , and extracts the relevant activation signals \mathbf{a} for the unit.

Algorithm 3: Spiking Handler asynchronous process.

InPorts: \mathbf{A}, \mathbf{s} ▷ Activation matrix and local spike vector
OutPorts: \mathbf{S}, \mathbf{a} ▷ Spike matrix and activation vector

```

1:  $\mathbf{s} \leftarrow \mathbf{0}_d, \mathbf{A} \leftarrow \mathbf{0}_{n \times d}$  ▷ Zero initialisation
2: while  $\text{RUNCONDITION}()$  do ▷ Asynchronous execution
3:    $\text{WAITFORINPUTS}()$  ▷ Handle asynchronous inputs
4:    $\mathbf{s}, \mathbf{A} \leftarrow \text{RECEIVE}()$ 
5:    $(\mathbf{S})_{i,:} \leftarrow \mathbf{s}$  ▷ Encode spikes
6:    $\mathbf{a} \leftarrow (\mathbf{A})_{i,:}$  ▷ Decode activations
7:    $\text{SEND}(\mathbf{S}, \mathbf{a})$ 

```

4.2.4 Sender and Receiver

These two processes perform the encoding and decoding tasks, similar to the Spike Handler process. However, we split them into dedicated processes because the information they handle is far more complex than binary arrays. On the one hand, the Sender broadcasts the local \mathbf{p} and f_p encoded into the i^{th} row of the position matrix $\mathbf{P} \in \mathbb{R}^{n \times d}$ and the fitness vector $\mathbf{f}_p \in \mathbb{R}^n$, respectively. On the other hand, the Receiver extracts the i^{th} neighbourhood's positions \mathbf{P} and fitness \mathbf{f}_{p_n} from \mathcal{P}_n and \mathbf{F}_n shared externally. This data is communicated with the rest of NHUs through the position and

fitness communication channels and depends on the floating point precision defined for the implementation. Lastly, Algorithm 4 and 5 detail the Sender and Receiver.

Algorithm 4: Sender asynchronous process.

InPorts: p, f_p \triangleright Candidate position and fitness
OutPorts: P, f_p \triangleright Position matrix and fitness vector
1: $P \leftarrow \mathbf{0}_{n \times d}, f_p \leftarrow \mathbf{0}_n$ \triangleright Zero initialisation
2: **while** RUNCONDITION() **do** \triangleright Asynchronous execution
3: WAITFORINPUTS() \triangleright Handle asynchronous inputs
4: $p, f_p \leftarrow \text{RECEIVE}()$
5: $(P)_{i,:} \leftarrow p, (f_p)_i \leftarrow f_p$ \triangleright Encode position and fitness
6: SEND(P, f_p)

Algorithm 5: Receiver asynchronous process.

InPorts: \mathcal{P}_n, F_n \triangleright Neighbourhood's positions and fitness
OutPorts: P_n, f_{p_n} \triangleright Positions and fitness of the i^{th} neighbourhood
1: $P_n \leftarrow \mathbf{0}_{m \times d}, f_{p_n} \leftarrow \mathbf{0}_m$ \triangleright Zero initialisation
2: **while** RUNCONDITION() **do** \triangleright Asynchronous execution
3: WAITFORINPUTS() \triangleright Handle asynchronous inputs
4: $\mathcal{P}_n, F_n \leftarrow \text{RECEIVE}()$
5: $P_n \leftarrow (\mathcal{P}_n)_{:,i}, f_{p_n} \leftarrow (F_n)_{:,i}$ \triangleright Decode information
6: SEND(P_n, f_{p_n})

4.3 Coordination Processes

This section completes the neurOptimiser's architectural description by detailing the coordination processes responsible for structuring information flow among NHUs.

4.3.1 High-Level Selector

This crucial coordination mechanism identifies and propagates the global best candidate g solution and its fitness f_g across all NHUs. Compared to the (low-level) Selector, the substantial difference between them lies in the number of solutions being analysed. Apart from that, both implement a greedy selection that, unlike the selector processes, must be preserved in the high-level selection, at least for single-objective optimisation problems. Algorithm 6 details the High-Level Selector process.

Algorithm 6: High-Level Selector asynchronous process.

InPorts: P, f_p \triangleright Candidate positions and their fitness values
OutPorts: g, f_g \triangleright Best candidate position and its fitness
1: **while** RUNCONDITION() **do** \triangleright Asynchronous execution
2: WAITFORINPUTS() \triangleright Synchronise incoming candidates
3: $P, f_p \leftarrow \text{RECEIVE}()$
4: $i_* \leftarrow \text{argmin}_{i \in \mathbb{N}_n} \{(f_p)_i\}$
5: **if** $(f_p)_{i_*} < f_g$ **or** $\neg \text{is_init}$ **then** \triangleright Greedy selection
6: $g \leftarrow (P)_{i_*}, f_g \leftarrow (f_p)_{i_*}$ \triangleright Update the best
7: $\text{is_init} \leftarrow \text{True}$
8: SEND(g, f_g)

4.3.2 Tensor Contraction Layer

This component transforms local spike emissions \mathcal{S} into distributed activation \mathcal{A} patterns across the SNN. This process emulates synaptic propagation by mapping the spike outputs of each NHU onto its predefined neighbourhood, which implements a structured interaction aligned with the spiking topology. Thus, \mathcal{A} is determined via the logical contraction operation adapted from [36], such as

$$(\mathcal{A})_{i,j} = \bigvee_{k=1}^n ((\mathcal{W})_{i,k,j} \wedge (\mathcal{S})_{k,j}), \forall i \in \mathbb{N}_n, j \in \mathbb{N}_d, \quad (24)$$

where $\mathcal{W} \in \mathbb{Z}_2^{n \times n \times d}$ is the weight tensor, which can be built simply by filling all the d slices using the adjacency matrix \mathcal{W}_s . After that, the process broadcasts the spiking influence without explicit synchronisation, which permits

each NHU to read binary activations from its connected peers. Algorithm 7 formalises the Tensor Contraction Layer process.

Algorithm 7: Tensor Contraction Layer asynchronous process.

InPorts: \mathcal{S} \triangleright Spike matrix
OutPorts: \mathbf{A} \triangleright Activation matrix
1: $(\mathcal{W})_{:,j} \leftarrow \mathbf{W}_s, \forall j \in \mathbb{N}_d$ \triangleright Initialise contraction weights
2: **while** RUNCONDITION() **do** \triangleright Asynchronous execution
3: WAITFORINPUTS()
4: $\mathcal{S} \leftarrow \text{RECEIVE}()$ \triangleright Handle asynchronous inputs
5: $\mathbf{A} \leftarrow \text{CONTRACT}(\mathcal{W}, \mathcal{S})$ \triangleright Compute activation using (24)
6: SEND(\mathbf{A})

4.3.3 Neighbour Manager

This process systematically aggregates positional information from neighbouring candidate solutions, which permits the structuring of local interactions within NeurOptimiser. Algorithm 8 specifies the procedure, which receives the particular best positions \mathbf{P} and their fitness \mathbf{f}_p , merged in the communication channel from those messages sent by NHUs, and processes them with an adjacency matrix \mathbf{W}_x describing the connections between NHUs. This matrix differs from \mathbf{W}_s , because it can be a real-valued matrix representing a weighted topology graph. However, we use a fixed ‘binary’ version of \mathbf{W}_x for simplicity.

Algorithm 8: Neighbour Manager asynchronous process.

InPorts: \mathbf{P}, \mathbf{f}_p \triangleright Positions matrix and fitness vector
OutPorts: $\mathcal{P}_n, \mathbf{F}_n$ \triangleright Neighbourhood positions and fitness values
1: $\mathbf{N}_i \triangleq \{j \in \mathbb{N}_n \mid (\mathbf{W}_x)_{i,j} = 1\}, \forall i \in \mathbb{N}_n$ \triangleright Get neighbours
2: $m \leftarrow \max_{i \in \mathbb{N}_n} \{\#\mathbf{N}_i\}$ \triangleright Max. number of neighbours
3: $\mathcal{P}_n \leftarrow \mathbf{0}_{m \times d \times n}, \mathbf{F}_n \leftarrow \mathbf{0}_{m \times n}$ \triangleright Initialise arrays
4: **while** RUNCONDITION() **do** \triangleright Asynchronous execution
5: WAITFORINPUTS()
6: $\mathbf{P}, \mathbf{f}_p \leftarrow \text{RECEIVE}()$ \triangleright Wait for position and fitness matrices
7: **for each** $i \in \mathbb{N}_n$ **do**
8: $(\mathcal{P}_n)_{\ell,:,i} \leftarrow (\mathbf{P})_{k\ell,:}, \forall k\ell \in \mathbf{N}_i, \ell \in \mathbb{N}_m$ \triangleright Get positions
9: $(\mathbf{F}_n)_{\ell,i} \leftarrow (\mathbf{f}_p)_{k\ell}, \forall k\ell \in \mathbf{N}_i, \ell \in \mathbb{N}_m$ \triangleright Get fitness
10: SEND($\mathcal{P}_n, \mathbf{F}_n$)

5 Methodology

This work followed a methodology accordingly to the novelty of the proposed approach. We designed and implemented the neurOptimiser, publicly available at neuroptimiser.github.io. Plus, all scripts, configuration files, and experimental results are freely available in [37]. The framework was developed based on Intel’s Lava NC framework [8] for CPU simulation and neuromorphic deployment targeting the Loihi 2 chip. All the experiments were conducted in Python v3.10 on a 48-core AMD EPYC 7642 CPU with 512 GB RAM, under Grid’5000 using Debian 5.10 x86-64 GNU/Linux. Grid’5000 is a testbed supported by a scientific interest group hosted by Inria, CNRS, RENATER, and several Universities, as well as other organisations (visit grid5000.fr for further information).

We adopted a three-fold experimental approach using the noiseless BBOB test suite from COCO and IOH [9, 38, 39], comprising 24 problems, six dimensionalities (2, 3, 5, 10, 20, and 40), and 15 instances per dimension. These are grouped as separable (separ), **f1–f5**; unimodal functions with low (lcond) and high (hcond) conditioning, **f6–f9** and **f10–f14**; and multimodal functions with either adequate (multi) or weak (mult2) global structure, **f15–f19** and **f20–f24**.

The first experiment characterised the principal behaviours of neurOptimiser implementations using the BBOB suite via IOH, with two dimensions, 30 NHUs, and $1000 \times d$ steps. The dynamic heuristic h_d was instantiated with the Linear and Izhikevich neuron models in (13) and (8) with random coefficients. All cases used 30 NHUs and the 4th-order Runge-Kutta method with $\Delta t = 0.01$. The spike-triggered heuristic h_s was set as Fixed (19) and DE/current-to-rand/1 (21b). Moreover, ϑ_j employed (16b); \mathbf{W}_s represented a bidirectional ring; \mathbf{W}_x was set random with $m = 10$ neighbours; \mathbf{x}_{ref} was defined as in (23a) with weights equal to 0.5; and φ_s used the ℓ_2 -norm based on (15a).

Subsequently, we carried out a confirmatory evaluation using the BBOB test suite from COCO. We selected the two best-performing Neuroptimiser variants from the preliminary analysis. An additional hybrid variant was created by blending these two models in a 50/50 proportion, producing a heterogeneous distribution of spiking models. The performance of these three neuroptimisers was systematically compared against baseline algorithm results from the literature.

The third experiment assessed the computational efficiency and scalability of the framework. We measured average runtime per step and NHU as a function of n and d using the same environment. In such a case, a hybrid-like neuroptimiser was implemented with the most computationally demanding setting, i.e., fully connected \mathbf{W}_s and \mathbf{W}_x , \mathbf{x}_{ref} as in (23b), and randomly assigned neuron models. Seven instances per function were considered, evaluated across 2, 10, 20, and 40 dimensions, using configurations with 30, 60, and 90 NHUs.

6 Results and Discussion

The initial set of experiments examines the internal behaviour of several neuroptimiser implementations. It isolates the effect of core dynamics and spike-triggered heuristic selection on population trajectories, state evolution, and spiking activity. All configurations were evaluated on the BBOB suite with one representative two-dimensional function per category.

Figure 6 depicts the evolution of the absolute error ε_r for these representative 2D problems under certain combinations of h_d and h_s heuristics. We chose to present the most descriptive ones for brevity, although the entire set of results can be consulted on [37]. In both the linear and Izhikevich models with the fixed spike-triggered rule, the mean and median error curves descend in discrete steps, interrupted by plateaus of limited progress. Considering that each grey curve corresponds to an individual NHU’s best error, most do not remain flat and instead exhibit gradual improvement throughout the search. This behaviour can be attributed to asynchronous progress and spike-driven information sharing. For both cores, employing the DE/current-to-rand/1 heuristic leads to an immediate reduction in population error variance, with statistical traces converging more rapidly. Under Izhikevich’s variant, the descent is sharper and the final error floor lower across all problem classes, particularly in **f15** and **f20**. This contrast is evident when compared to the curves obtained with the fixed h_s .

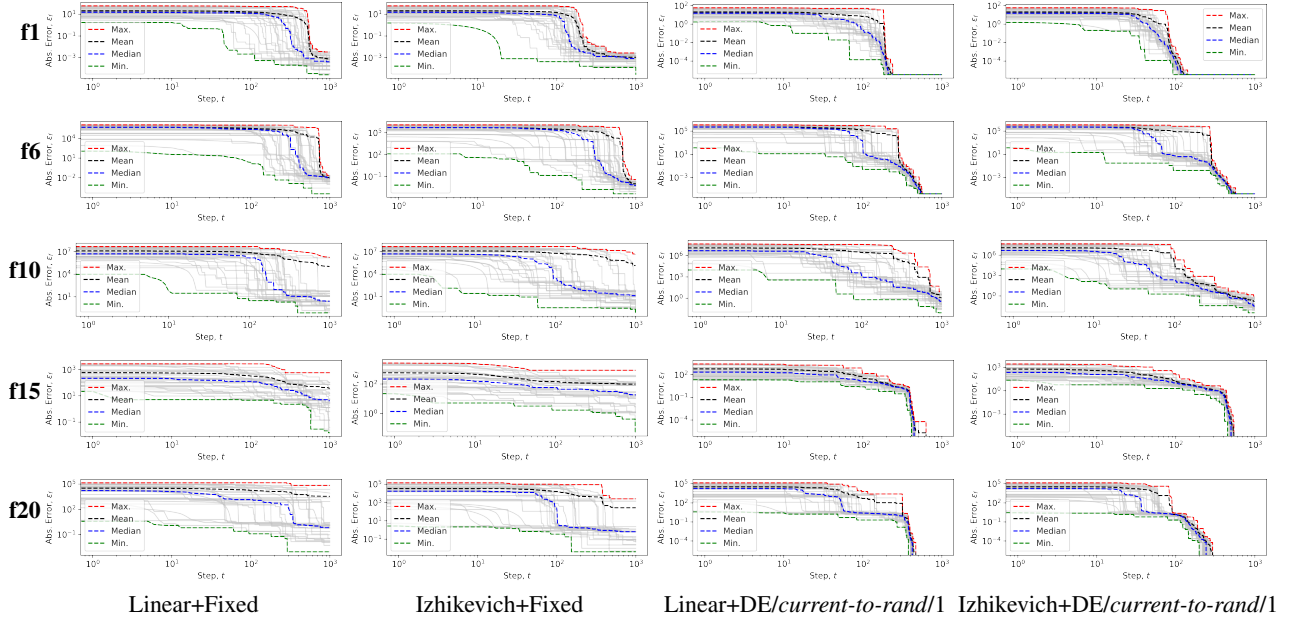


Figure 6: Absolute error $\varepsilon_f = |f(\mathbf{p}_i) - f(\mathbf{x}_*)|$ over 1000 steps for the first 2D BBOB function of each different problem subgroup; i.e., *separ*, *1cond*, *hcond*, *multi*, and *mult2*. Each row stands for a function f_k from the BBOB suite. Each column corresponds to neuroptimisers (h_d+h_s) implemented using the Linear and Izhikevich models as h_d , and the Fixed and DE/current-to-rand/1 rules as h_s .

Subsequently, Figure 7 presents the temporal evolution of best-so-far positions ($x_1, x_2 \in \mathbf{p}_i^t$) for each neuroptimiser configuration. Each vertical segment corresponds to an NHU whose \mathbf{p}_i^t remains unchanged for several steps. Considering that the dashed black and red lines represent the target (\mathbf{x}_*) and the global best (\mathbf{g}^t) position evolution,

respectively, we then verify that all the implementations approached the target position closely. From these plots, we notice that the neuroOptimisers using fixed h_s exhibit gradual and staircase-like positional shifts, accompanied by extended static segments. These patterns are most pronounced in the Linear model and for ill-conditioned (**f10**) or multimodal (**f15**) landscapes. Besides, Izhikevich dynamics produce abrupt transitions and more localised position clustering, especially during steps of collective firing. This is explained by the nature of linear systems, which tend to move smoothly in phase space, even when exhibiting swift dynamics dictated by nodal equilibrium points (cf. Figure 3). Such a dynamic represents an excellent mechanism for exploitation courses. It is observed as static best positions, mainly on fixed rules, coinciding with those slow error plateaux in Figure 6. In contrast, the Izhikevich model mostly sweeps only the membrane potential variable, while the auxiliary variable remains invariant (cf. Figure 2). Moreover, DE/current-to-rand/1 as h_s induces frequent and spatially coordinated advances. This rule drives the entire population towards the target position with vertical transitions and early trajectory collapse. With these implementations, we notice that neuroOptimiser using traditional spiking neuron models, such as LIF and Izhikevich in (6) and (7), may be insufficient for effectively searching within complex problem landscapes. While the problems are simple, these results highlight the neuroOptimiser’s capacity to generate distinct behaviours and suggest that certain h_d+h_s combinations may require finer tuning to escape stagnation. It is worth mentioning that regarding the evolution of \mathbf{g}^t towards \mathbf{x}_* in Figure 7, we can infer that those flatlines in Figure 6, at least corresponding to the minimum value, can be primarily due to floating point precision issues.

Although the best positions provide interesting information about the evolutionary process, they are inherently limited by the greedy nature of this feature. For that reason, we analyse the portraits of state variables ($v_{1,j}, v_{2,j} \in \mathbf{v}_j$) for all steps and all NHUs, as Figure 8 displays. In this case, we only chose the DE/current-to-rand/1 variant for both dynamic models to illustrate the different behaviours controlled mainly by h_d . While the linear model searches using two degrees of freedom, which is evident in trajectories describing perceptible spiral dynamics, the Izhikevich model focuses mainly on sweeping the membrane potential variables horizontally. In these portraits, the chosen \mathbf{x}_{ref} makes $v_{1,1} = v_{1,2} = 0$ corresponds to a centring of the neuromorphic representation in the phase plane for each component. When we compare the state transitions to the positions shown in Figure 7, a direct correspondence is evident. In the linear case, the broad exploration of the state space produces scattered and irregular position updates. In the Izhikevich case, the horizontal banding of state trajectories leads to periods where many positions change abruptly at the same step. This results in tight position clustering and collective shifts in the population.

Lastly, we complement the analysis of the internal neuroOptimiser dynamics by examining the spike activity generated during the search. Figure 9 displays the temporal distribution of spike counts per NHU for the previously analysed configurations. In all the spiking maps, we notice that slight triangular patterns arise on the first steps from the bidirectional ring topology implemented for the SNN via \mathbf{W}_s . This spike event propagation is more evident on NHUs using the linear model because of their smooth dynamic in the space state discussed in Figure 8. For the Izhikevich configuration, frequent vertical bands reflect near-simultaneous firing of multiple units, caused by the nonlinear dynamics. In the case of **f1**, the Izhikevich model reaches the shrunk spiking condition set \mathcal{S} earlier than the linear variant, reflecting a faster contraction of the state variables and an earlier onset of collective spiking. Besides, for **f10** from the ill-conditioned functions, we observe that the spike activity is more fragmented in both configurations, with fewer instances of broad synchrony across the population. The presence of persistent diagonal, but narrow, bands in the linear case and irregular vertical patterns in the Izhikevich case indicates that units reach the spiking condition at different times. This is consistent with slower and less coordinated progress in both state and position trajectories for this challenging landscape (cf. Figure 7 and 8). From this analysis, we corroborate that the spiking condition set directly adapts the behaviour of each NHU during the search by controlling when rules are triggered.

The subsequent experiment comprised three neuroOptimiser variants across all BBOB function classes and dimensionalities. In this experiment, Neuropt-Lin and Neuropt-Izh correspond to those implementations using the Linear and Izhikevich models as h_d and DE/current-to-rand/1 as h_s , as examined in the previous section. Neuropt-Hyb denotes a heterogeneous variant comprising equal proportions of both core models within the population.

Figure 10 displays the Empirical Cumulative Distribution Functions (ECDFs) of normalised runtimes for all function groups and all dimensions. In general, we notice that all variants achieve a high fraction of solved function–target pairs for low-dimensional cases (i.e., up to 5D) with a reduced evaluation budget. In the intermediate dimensionality, Neuropt-Izh consistently exhibits faster convergence than Neuropt-Lin. At the same time, Neuropt-Hyb maintains performance comparable to the best homogeneous variant and reveals increased robustness as dimensionality grows. For 20D and 40D, all approaches show reduced success, with the fraction of solved pairs flattening well below one. The plateaux observed in the results arise from the constrained evaluation budget employed in the simulations rather than from any intrinsic limitation of the neuroOptimiser variants. This effect becomes more evident in the 20D and 40D settings. Despite this, the overall trend across dimensions reveals robust and scalable convergence, confirming the potential of the proposed spike-driven asynchronous mechanisms for optimisation problems.

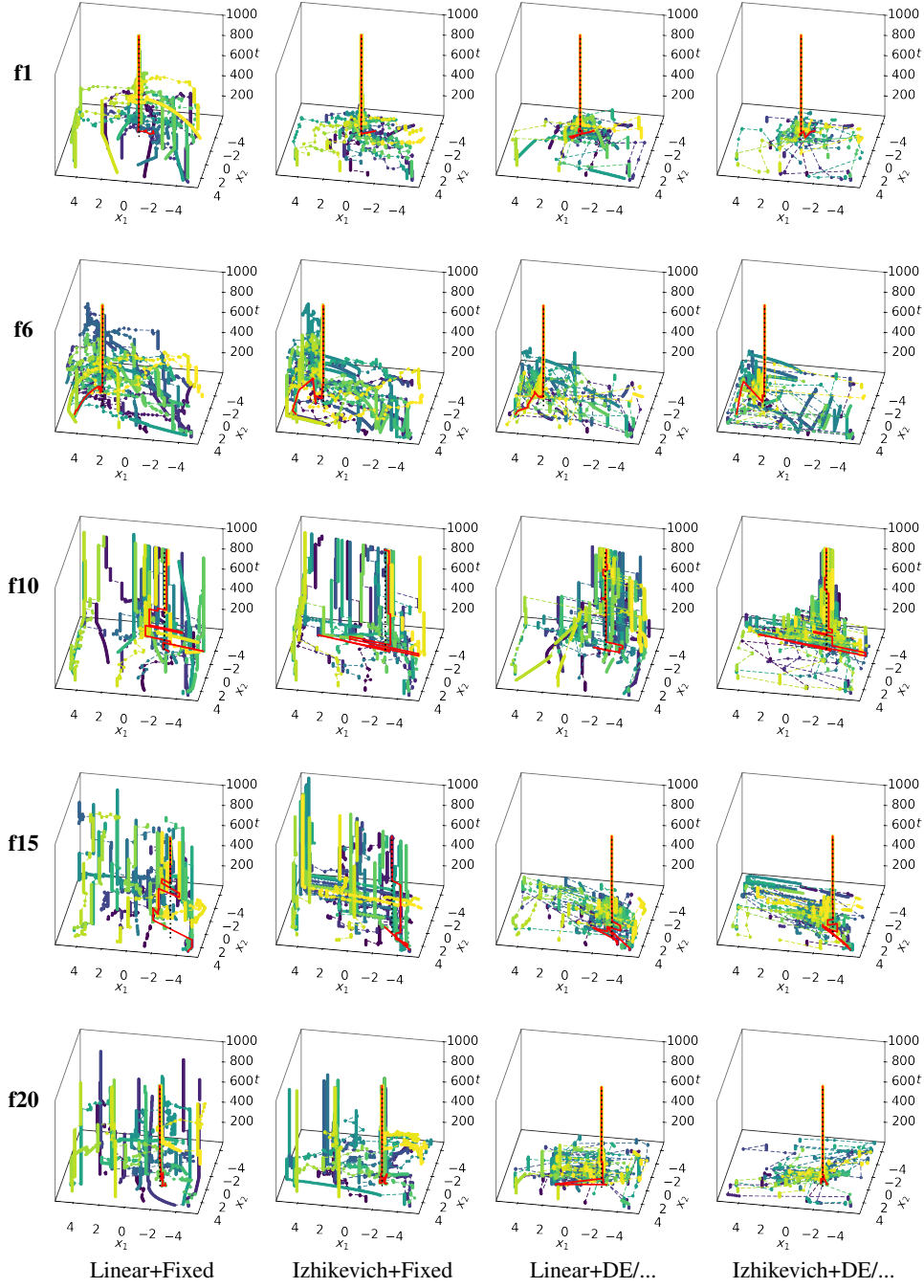


Figure 7: Particular best positions ($x_1, x_2 \in \mathbf{p}_i^t$) of a 1000-step simulation with two NeurOptimisers with 30 NHUs searching on 2D problem domains. Each row stands for a function f_k from the BBOB suite. Each column corresponds to neurOptimisers (h_d+h_s) implemented using the Linear and Izhikevich models as h_d , and the Fixed and DE/*current-to-rand*/1 rules as h_s . Dashed black and red lines mark the target and global best.

This trend is further clarified in Figure 11, which quantifies the Expected Running Time (ERT) loss ratio of each variant relative to the BBOB 2009 reference. Recall that ERT quantifies the expected number of function evaluations required by an algorithm to reach a given target function value [9]. In 5D, all neurOptimiser variants maintain loss ratios near or below unity across most budgets. This verifies that the observed performance in low dimensions matches established benchmarks. As dimensionality increases to 20D, the dispersion in loss ratios grows and median values shift above one, consistent with the plateaux seen previously. This increase is attributable to the constrained evaluation

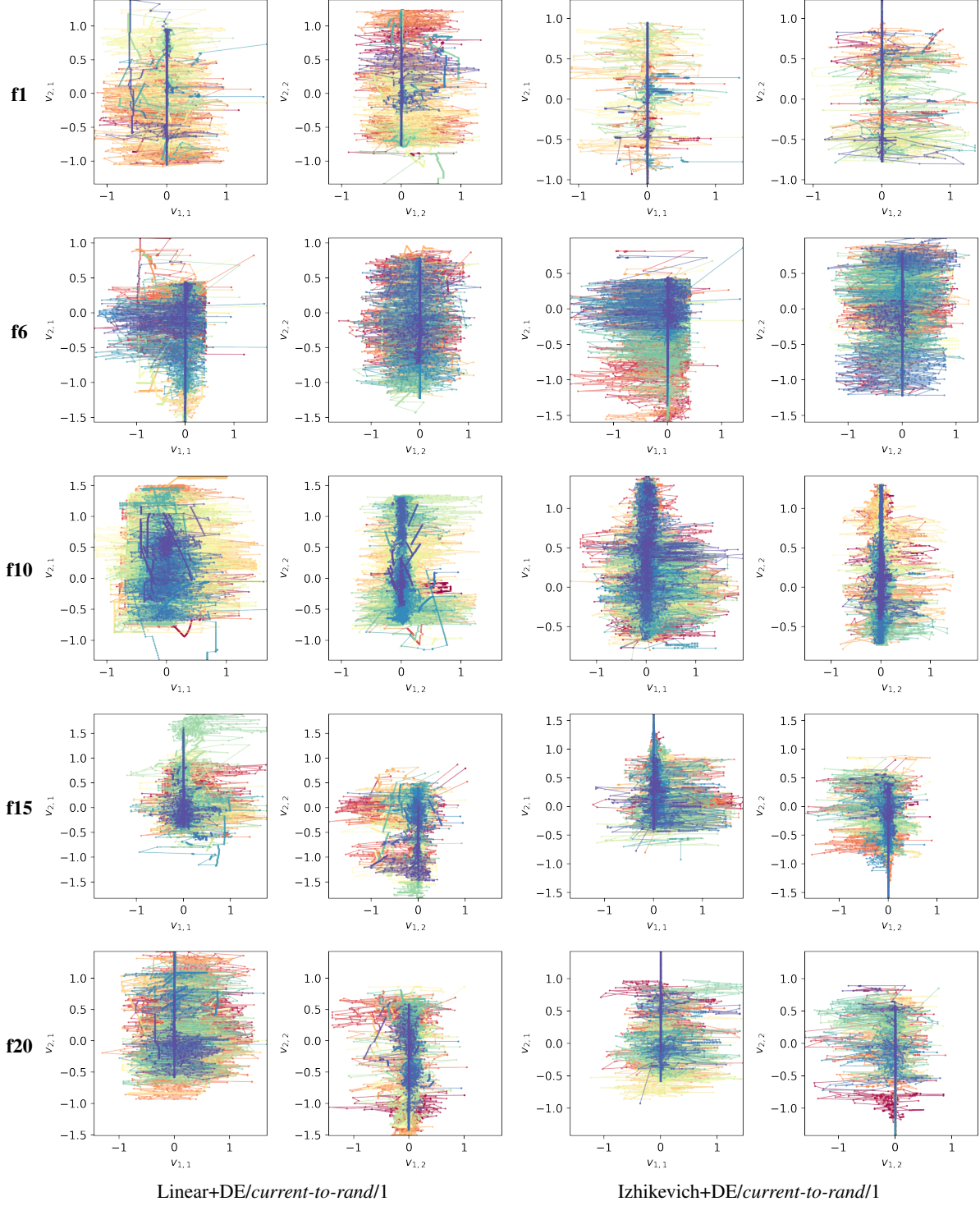


Figure 8: Portraits of neuromorphic state variables ($v_{1,j}, v_{2,j} \in \mathbf{v}_j^t, \forall j$) of a 1000-step simulation with two NeurOptimisers with 30 NHUs searching on 2D problem domains. Each row stands for a function f_k from the BBOB suite. Each column corresponds to neurOptimisers (h_d+h_s) implemented with the Linear and Izhikevich models as h_d , and DE/current-to-rand/1 as h_s .

budget rather than algorithmic stagnation, as hard instances remain unsolved within the allocated steps. Occasionally, high outliers appear when challenging instances are not solved within the budget, causing the ERT loss ratio to

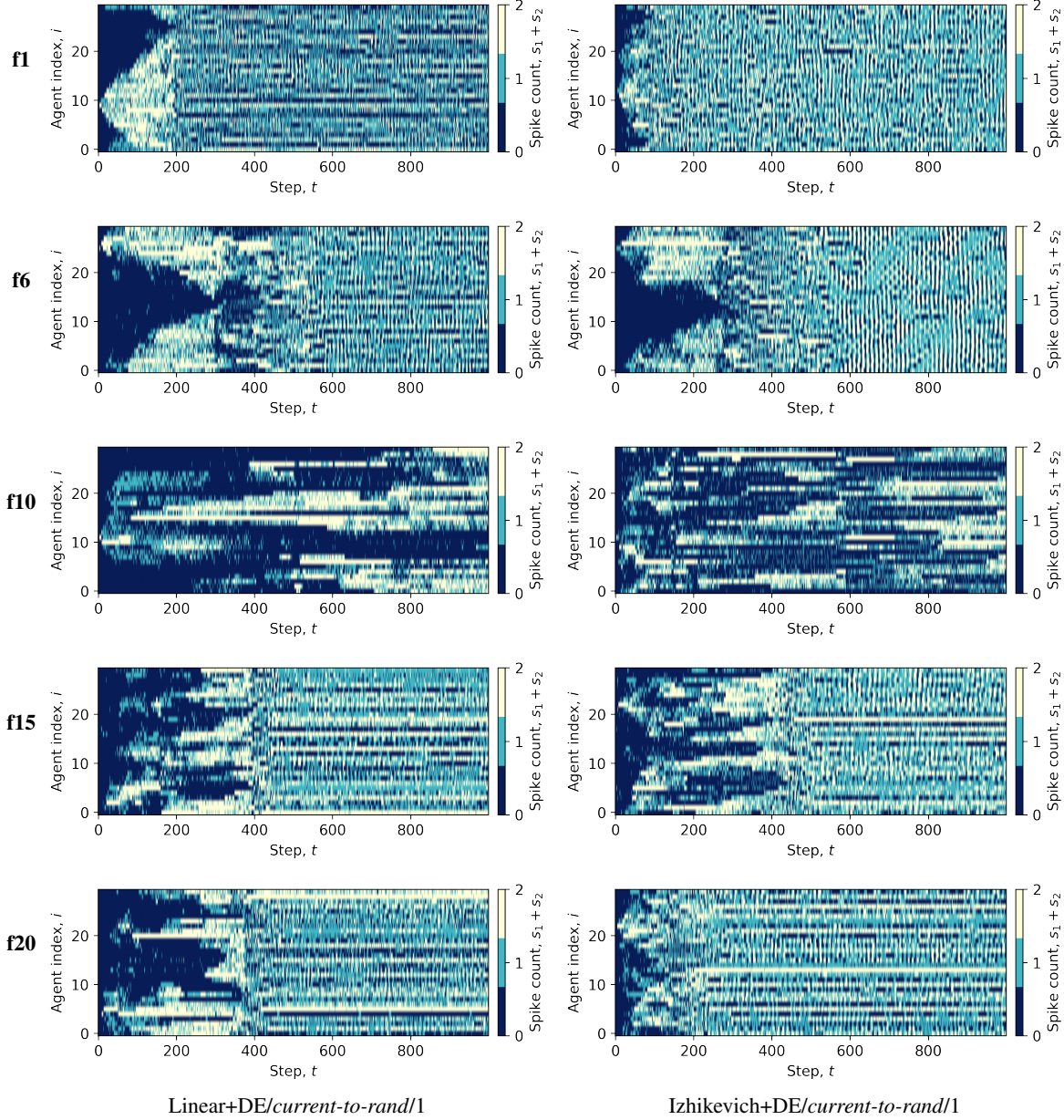


Figure 9: Spiking signal count ($s_1 + s_2$) of a 1000-step simulation with two NeurOptimisers with 30 NHUs, each one with an index i , searching on 2D problem domains. Each row stands for a function f_k from the BBOB suite. Each column corresponds to neurOptimisers (h_d+h_s) implemented with the Linear and Izhikevich models as h_d , and DE/current-to-rand/1 as h_s .

spike for those cases [9]. Hence, these results support that the spike-driven approach retains competitive efficiency in moderate dimensions and remains robust even as problem complexity increases.

Figure 12 details the ECDFs of normalised runtimes for all neurOptimiser variants, RANDOMSEARCH auger noiseless [40], and the BBOB 2009 reference, split down by function subgroup and dimension. In line with the global trends reported previously, both Neuropt-Izh and Neuropt-Hyb achieve rapid convergence and high fractions of solved pairs for separable (separ) and low-conditioned (1cond) functions up to 10D, closely tracking the BBOB 2009 reference and significantly outperforming RANDOMSEARCH. On high-conditioned (hcond) and multimodal (multi and multi2) problems, the fraction of solved pairs decreases as dimension increases, with the difference becoming most pronounced in 20D. For these tough groups, Neuropt-Hyb exhibits increased robustness, often maintaining higher solved fractions than either of the homogeneous variants, consistent with the expected benefits of population diversity

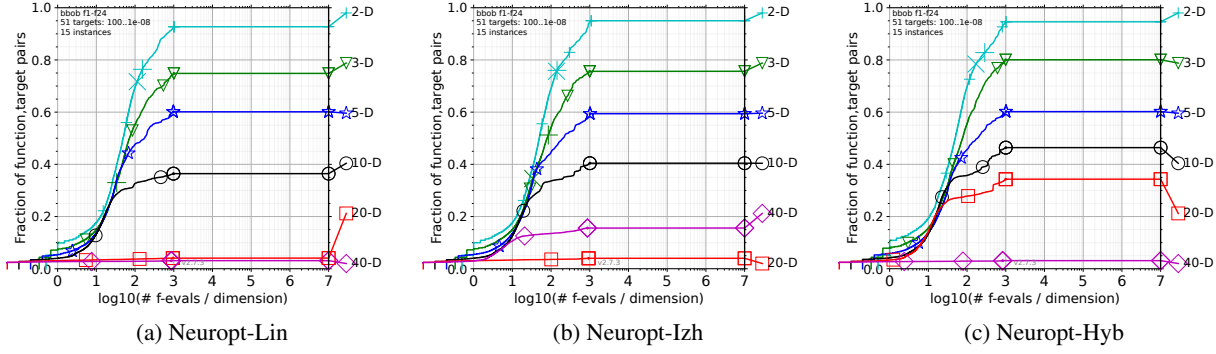


Figure 10: Empirical Cumulative Distribution Functions (ECDFs) of normalised runtimes for the three neurOptimiser implementations on the BBOB test suite. Each curve shows the fraction of function-target pairs solved as a function of f -evaluations per dimension, for 51 targets $10^{[-8..2]}$ over all functions, instances, and dimensions. Higher curves indicate more efficient convergence. Data produced with COCO v2.7.3

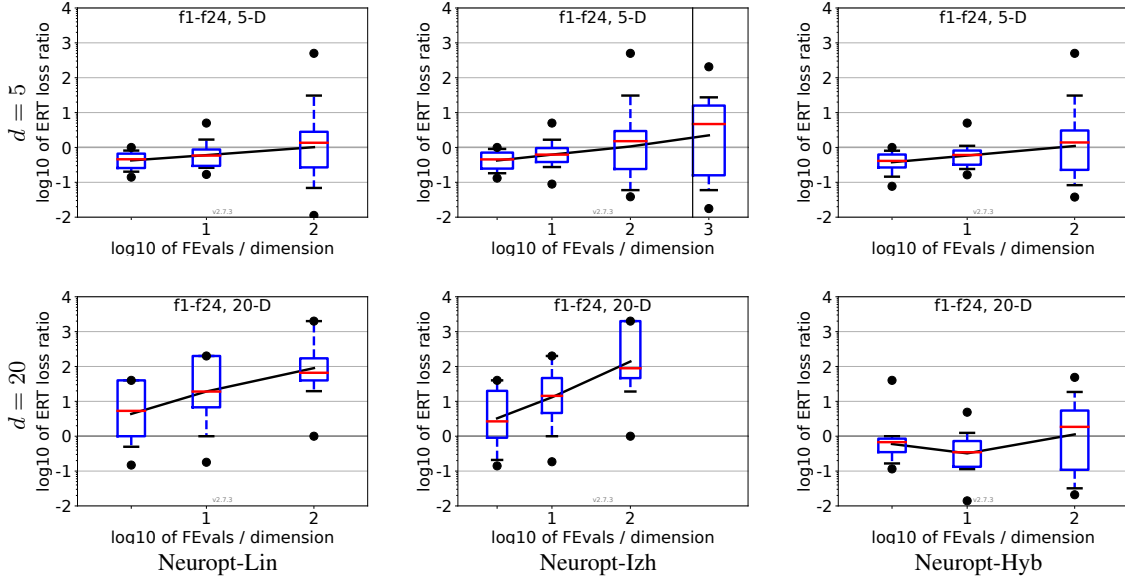


Figure 11: Expected Running Time (ERT) loss ratio vs. the budget in number of f -evaluations per dimension. For each budget, the ERT to reach the best target f -value is divided by the ERT of the best BBOB 2009 method for the same target. Lines show the geometric mean; box-whiskers indicate 25-75% (box), 10-90% (caps), and min-max (points). The vertical line marks the evaluation budget limit for this subset. Data produced with COCO v2.7.3

in challenging landscapes. Across all scenarios, RANDOMSEARCH displays a steady and gradual increase, but rarely reaches the highest fractions of solved pairs within the available budget, higher than the one used by our approach.

It is worth noting that the objective of this study is to demonstrate the viability of spike-driven heuristics as a general optimisation framework, rather than to achieve state-of-the-art performance. Instead, the comparative analysis is intended to confirm that the neurOptimiser framework achieves competitive results even when operating under a limited evaluation budget, reduced population sizes, and without extensive parameter fine-tuning. There is a massive room for improvement and future research. For this reason, we employed results from a random search implementation and the best BBOB 2009 algorithm as the lower and upper benchmarks to establish the performance bounds. As previously noticed, the flat lines observed in the ECDFs, especially for high-dimensional and complex functions, primarily reflect the restrictive evaluation budget rather than an intrinsic limitation of the neurooptimiser approach. These results corroborate the analysis in Figure 10 and 11, supporting the observation that performance boundaries are shaped by resource allocation and problem complexity.

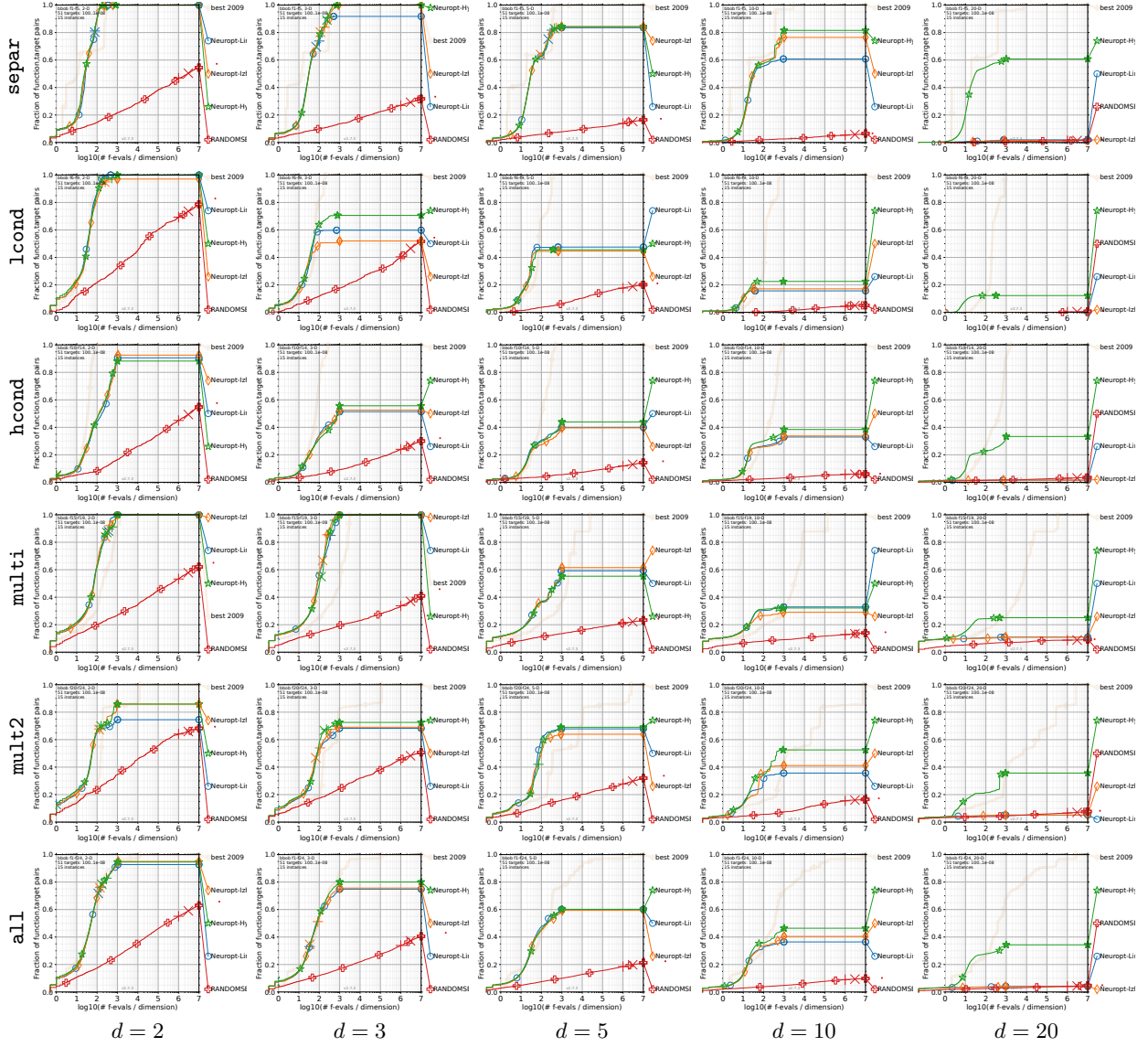


Figure 12: Bootstrapped Empirical Cumulative Distribution Function (ECDF) of the number of f -evaluations divided by dimension for 51 targets in $10^{[-8..2]}$ across all function subgroups, with 15 instances per dimension, shown for dimensions 2, 5, 10, and 20. The best algorithm from BBOB 2009 is shown as a light, thick reference line. Legend: \circ : Neuropt-Hyb, \diamond : Neuropt-Izh, \star : Neuropt-Lin, $+$: RANDOMSEARCH [40]. Data produced with COCO v2.7.3

Furthermore, Table 1 complements the convergence analysis by providing detailed ERT for the first function of each BBOB subgroup in 5D. (The complete dataset can be found in [37].) For **f1**, all neuroOptimiser configurations reach the majority of targets in most trials, with Neuropt-Lin and Neuropt-Hyb closely matching or exceeding the BBOB 2009 baseline for all attainable targets. However, it is clear that none of the neuroOptimiser variants consistently achieves the final targets. On **f6** (lcond), only the first two targets are reliably reached by all neuroOptimisers. For **f10** (hcond), all configurations stagnate at coarse targets, consistent with the previous ECDF trends. In the weakly structured subgroup, both Neuropt-Lin and Neuropt-Hyb report the best ERTs on **f15** for all targets except the final one, with ERT ratios below one and a clear improvement over RANDOMSEARCH for that target. For **f20**, Neuropt-Lin exhibits good scalability, solving the initial targets in all trials, surpassing RANDOMSEARCH, with Neuropt-Lin showing stable and consistently lower ERTs. These results corroborate the ECDF and ERT analyses and confirm that while homogeneous neuroOptimisers can excel in some instances, Neuropt-Hyb provides more robust performance across problem types.

Table 1: Expected runtime (ERT, in f -evaluations) for each algorithm and target, normalised by the best BBOB 2009 ERT in 5D. Each cell depicts the ERT ratio, along with the half-difference between the 10th and 90th percentiles (bootstrapped) in parentheses. Reference ERTs are in the first row. #succ is the number of successful trials for the final target $f_{\text{opt}} + 10^{-8}$. Italics indicate medians where the target was not reached. Stars mark statistically best entries; \uparrow flags some worse than the reference. Bold indicates best results. Data produced with COCO v2.7.3

Δf_{opt}	10^1	10^0	10^{-1}	10^{-2}	10^{-3}	10^{-5}	10^{-7}	#succ
f1	11	12	12	12	12	12	12	15/15
Neuropt-Lin	0.66(0.4)	2.1(0.2)	3.4(0.4)	4.2(0.5)	5.1(0.6)	6.8(0.8)	68(171)	4/15
Neuropt-Izh	0.79(0.6)	2.1 (0.5)	3.2 (0.5)	4.1 (0.5)	5.0 (0.6)	6.6 (0.8)	62(116)	5/15
Neuropt-Hyb	0.57 (0.5)	2.2(0.5)	3.4(0.5)	4.4(0.7)	5.2(0.8)	6.7(0.8)	29 (8)	5/15
RANDOMSEARCH	7.5(10)	1698(1877)	6.9e5(1e6)	∞	∞	∞	∞ 5e6	0/15
f6	114	214	281	404	580	1038	1332	15/15
Neuropt-Lin	0.34 (0.1) \uparrow 0	0.47(0.2)	0.69(0.1)	∞	∞	∞	∞ 2	0/15
Neuropt-Izh	0.41(0.1) \uparrow 0	0.43 (0.1)	∞	∞	∞	∞	∞ 2	0/15
Neuropt-Hyb	0.34(0.1) \uparrow 0	0.45(0.2) \uparrow 1	0.46 (0.1)	∞	∞	∞	∞ 2	0/15
RANDOMSEARCH	303(425)	5.7e4(7e4)	∞	∞	∞	∞	∞ 5e6	0/15
f10	349	500	574	607	626	829	880	15/15
Neuropt-Lin	2.1 (2)	∞	∞	∞	∞	∞	∞ 2	0/15
Neuropt-Izh	∞	∞	∞	∞	∞	∞	∞ 2	0/15
Neuropt-Hyb	3.3(2)	∞	∞	∞	∞	∞	∞ 2	0/15
RANDOMSEARCH	∞	∞	∞	∞	∞	∞	∞ 5e6	0/15
f15	511	9310	19369	19743	20073	20769	21359	14/15
Neuropt-Lin	0.21(0.1) \uparrow 0	0.19 (0.1)	0.10 (0.1)	0.10 (0.1)	0.10 (0.1)	0.09(0.1)	0.18(2e-3)	0/15
Neuropt-Izh	0.23(0.1) \uparrow 0	0.20(0.1)	0.11(0.1)	0.11(0.1)	0.11(0.1)	0.07 (0.0)	∞ 2	0/15
Neuropt-Hyb	0.18 (0.1) \uparrow 0	0.26(0.2)	0.12(0.1)	0.12(0.1)	0.12(0.1)	0.11(0.0)	0.08 (1e-3)	0/15
RANDOMSEARCH	6853(7246)	∞	∞	∞	∞	∞	∞ 5e6	0/15
f20	16	851	38111	51362	54470	54861	55313	14/15
Neuropt-Lin	0.98 (0.3)	0.29 (0.2) \uparrow 0	9.8e-3 (3e-3)	7.5e-3 (2e-3)	7.3e-3 (2e-3)	7.6e-3 (2e-3)	0.01(7e-3)	4/15
Neuropt-Izh	1.1(0.3)	0.46(0.2)	0.01(7e-3)	0.01(5e-3)	0.01(5e-3)	9.4e-3(2e-3)	0.01 (1e-3)	3/15
Neuropt-Hyb	1.1(0.2)	0.34(0.1) \uparrow 0	0.01(6e-3) \uparrow 1	0.01(5e-3) \uparrow 1	0.01(4e-3) \uparrow 1	0.01(5e-3) \uparrow 1	0.02(0.0)	5/15
RANDOMSEARCH	29(40)	9230(1e4)	∞	∞	∞	∞	∞ 5e6	0/15

Last but not least, to evaluate the computational efficiency of the proposed framework, we measured the average runtime per step and NHU across varying numbers of units and problem dimensionalities. Figure 13 displays these average runtimes varying the number of NHUs n and problem dimensionality d . We observe that the computational cost increases linearly with both parameters, confirming the expected scaling of asynchronous and event-driven architectures. Even for the most significant tested values, the per-unit runtime remains below 12 ms, with the slope increasing moderately as d grows due to the added cost of spike propagation and local updates. Across all experiments, we notice that the relative variability (σ/μ) remains consistently low, indicating the regularity of the implementations. These results also validate the computational efficiency of the proposed framework and align with the behaviour reported in NC literature [30, 41], where event-driven models are known to maintain low latency and power consumption, especially under sparse activity. As all experiments were conducted as CPU simulations with the most demanding connectivity settings, we anticipate further gains when deployed on dedicated neuromorphic hardware, where locality and event-driven computation can be fully leveraged.

Additionally, Figure 13 also presents the power estimates for all evaluated settings in parentheses above each violin. We assessed these values as upper bounds on the power consumption of our framework when deployed on Intel’s Loihi chip [41]. This estimation accounts for the number of synaptic events ($N_{\text{syn}} = n(n-1)md$), neuron updates, and spike transmissions per step. Using Loihi’s reported costs of 23.6 pJ per synaptic event, 81 pJ per neuron update, and 8.7 pJ per spike, the total energy per step is given by $E_{\text{step}} = 23.6 N_{\text{syn}} + 89.7n$ pJ. With a simulation time step of $\Delta t_{\text{sim}} = 0.5$ ms, the average power is computed as $P_{\text{avg}} = E_{\text{step}}/\Delta t_{\text{sim}}$. Therefore, for the worst-case configuration tested ($n = 90$, $d = 40$, $m = 89$), this yields $E_{\text{step}} \approx 0.67$ mJ and $P_{\text{avg}} \approx 1.35$ W. In practice, the actual

power consumption will be lower due to sparse spike activity (Figure 9) and the event-driven design of Loihi, which ensures that inactive units consume negligible energy.

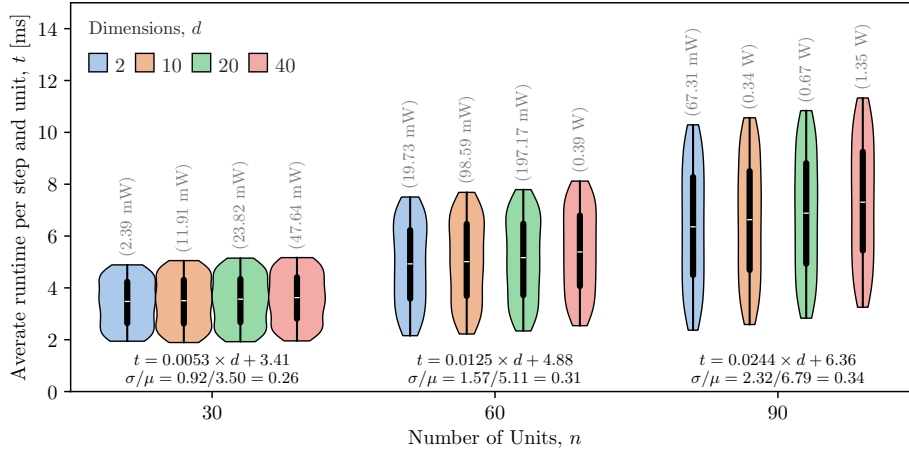


Figure 13: Average runtime per step and unit (t [ms]) as a function of the number of NHUs n and dimensionality d . Problem instances were evaluated across 2, 10, 20, and 40 dimensions, using configurations with 30, 60, and 90 NHUs. Violin plots display the distribution of per-unit runtimes across trials. Mean runtime (white dot), estimated power consumption (in parentheses), linear regression equations, and σ/μ ratios are reported for each setting.

7 Conclusion

This work addressed the challenge of scalable, low-power optimisation by introducing NeurOptimiser, a framework that combines population-based metaheuristics and neuromorphic computing. This approach performs an evolutionary search using only asynchronous, spike-triggered dynamics, eliminating the need for central coordination or surrogate modelling. We established its foundational components, comprising a population of NHUs that encode candidate solutions and evolve their state through event-driven dynamics. Each unit receives input from neighbour processes via spike events, with state transitions triggered by local conditions only using a dynamic h_d and spike-triggered h_s heuristics. We specified how dynamic models, either discrete or continuous, can be defined as h_d , as well as evolutionary mechanisms such as perturbation and selection are embedded as h_s . Moreover, we detailed all the other relevant components to bear in mind when implementing this approach, such as the spiking condition that triggers transitions, the bidirectional transformation for encoding and decoding candidate solutions, and the thresholding mechanism, among others.

We implemented and tested several NeurOptimiser variants, considering combinations mainly of two-dimensional dynamic systems such as linear and Izhikevich models as h_d , and the fixed and DE/current-to-rand heuristics as h_s . For testing, we employed Intel’s Lava platform, targeting the Loihi 2 chip, for materialising our approach and the noiseless BBOB suite up to 40 dimensions. Results showed that the neurOptimiser approaches reliably converged on separable, unimodal, and moderately conditioned problems, while matching reference methods in low and moderate dimensions. Plus, we found that performance decreased and variance increased on high-dimensional, multimodal, and ill-conditioned functions under tight evaluation budgets. Such an outcome highlights the limitations of fixed spike-triggered rules and uniform model assignment, as homogeneous configurations are often outperformed by the heterogeneous variant on more complex problems. Recall that homogeneous variants used the same dynamic model and heuristic for all units, while the heterogeneous variant blended linear and Izhikevich cores within the NHUs. Furthermore, we observed a linear scaling of runtime and resource consumption with increasing population size and dimensionality, with per-unit runtimes under 12 ms and milliwatt-level power estimates. We confirmed the suitability of the architecture for practical NC hardware deployments.

This framework stands for the first complete and reproducible integration of neuromorphic heuristic-based optimisers. It constitutes a principled path toward low-energy, real-time, and fully decentralised optimisation. For future work, further progress requires adaptive rule selection, increased model heterogeneity, and large-scale deployment on physical NC hardware. Additionally, we plan to integrate advanced dynamic models, extend support to multi-objective and large-scale optimisation, and enable real-time evaluation in embedded environments.

Acknowledgments

The authors utilised OpenAI’s ChatGPT-4o and Grammarly for language polishing under human supervision. No AI was used for scientific ideas, data analysis, or interpretation. The authors remain fully responsible for the manuscript.

References

- [1] E.-P. Li, H. Ma, M. Ahmed, T. Tao, Z. Gu, M. Chen, Q. Chen, D. Li, and W. Chen, “An electromagnetic perspective of artificial intelligence neuromorphic chips,” *Electromagnetic Science*, vol. 1, no. 3, p. 18, 2023.
- [2] Sanaullah, S. Koravuna, U. Rückert, and T. Jungeblut, “Exploring spiking neural networks: a comprehensive analysis of mathematical models and applications,” *Frontiers in Computational Neuroscience*, vol. 17, p. 1215824, 2023.
- [3] J. D. Nunes, M. Carvalho, D. Carneiro, and J. S. Cardoso, “Spiking Neural Networks: A Survey,” *IEEE Access*, vol. 10, p. 60738–60764, 2022.
- [4] D. Ivanov, A. Chezhegov, M. Kiselev, A. Grunin, and D. Larionov, “Neuromorphic artificial intelligence systems,” *Frontiers in Neuroscience*, vol. 16, p. 959626, 2022.
- [5] Z.-H. Zhan, L. Shi, K. C. Tan, and J. Zhang, “A survey on evolutionary computation for complex continuous optimization,” *Artificial Intelligence Review*, vol. 55, no. 1, pp. 59–110, 2022.
- [6] J. Liu, R. Sarker, S. Elsayed, D. Essam, and N. Siswanto, “Large-scale evolutionary optimization: A review and comparative study,” *Swarm and Evolutionary Computation*, vol. 85, p. 101466, 2024.
- [7] E. Talbi, “Neuromorphic-based metaheuristics: A new generation of low power, low latency and small footprint optimization algorithms,” 2025. [Online]. Available: <https://arxiv.org/abs/2505.16362>
- [8] Intel Neuromorphic Computing Lab, “Lava: A software framework for neuromorphic computing,” <https://github.com/lava-nc>, 2023, accessed: 2025-03-28.
- [9] N. Hansen, A. Auger, R. Ros, O. Mersmann, T. Tušar, and D. Brockhoff, “COCO: A platform for comparing continuous optimizers in a black-box setting,” *Optimization Methods and Software*, vol. 36, pp. 114–144, 2021.
- [10] Z. Lin and Z. Fan, “A ferroelectric memristor-based transient chaotic neural network for solving combinatorial optimization problems,” *Symmetry*, vol. 15, no. 1, p. 59, 2022.
- [11] H. Kim, M. Kim, A. Lee, H. Park, J. Jang, J. Bae, I. M. Kang, E. Kim, and S. Lee, “Organic memristor-based flexible neural networks with bio-realistic synaptic plasticity for complex combinatorial optimization,” *Advanced Science*, vol. 10, no. 19, p. 2300659, 2023.
- [12] A. S. Lele, M. Chang, S. D. Spetalnick, B. Crafton, A. Raychowdhury, and Y. Fang, “Neuromorphic swarm on RRAM compute-in-memory processor for solving QUBO problem,” *2023 60th ACM/IEEE Design Automation Conference (DAC)*, vol. 00, pp. 1–6, 2023.
- [13] A. Pierro, P. Stratmann, G. A. F. Guerra, S. Risbud, T. Shea, A. R. Mangalore, and A. Wild, “Solving QUBO on the Loihi 2 Neuromorphic Processor,” *arXiv*, 2024.
- [14] K. Roy, A. Jaiswal, and P. Panda, “Towards spike-based machine intelligence with neuromorphic computing,” *Nature*, vol. 575, no. 7784, pp. 607–617, 2019.
- [15] S. Shen, R. Zhang, C. Wang, R. Huang, A. Tuerhong, Q. Guo, Z. Lu, J. Zhang, and L. Leng, “Evolutionary spiking neural networks: A survey,” *arXiv*, 2024. [Online]. Available: [10.48550/arxiv.2406.12552](https://arxiv.org/abs/10.48550/arxiv.2406.12552)
- [16] C. D. Schuman, J. P. Mitchell, R. M. Patton, T. E. Potok, and J. S. Plank, “Evolutionary optimization for neuromorphic systems,” in *Proceedings of the 2020 Annual Neuro-Inspired Computational Elements Workshop*, ser. NICE’20. New York, NY, USA: ACM, 2020. [Online]. Available: <https://doi.org/10.1145/3381755.3381758>
- [17] C. D. Schuman, S. R. Young, B. P. Maldonado, and B. C. Kaul, “Real-time evolution and deployment of neuromorphic computing at the edge,” in *2021 12th International Green and Sustainable Computing Conference (IGSC)*. IEEE, 2021, pp. 1–8.
- [18] Y. Fang, Z. Wang, J. Gomez, S. Datta, A. I. Khan, and A. Raychowdhury, “A swarm optimization solver based on ferroelectric spiking neural networks,” *Frontiers in Neuroscience*, vol. 13, p. 855, 2019.
- [19] T. Sasaki and H. Nakano, “Swarm intelligence algorithm based on spiking neural-oscillator networks, coupling interactions and search performances,” *Nonlinear Theory and Its Applications, IEICE*, vol. 14, no. 2, p. 267–291, 2023.

- [20] A. Javanshir, T. Nguyen, M. Mahmud, and A. Kouzani, “Advancements in algorithms and neuromorphic hardware for spiking neural networks,” *Neural Computation*, vol. 34, no. 6, p. 1289–1328, 2022.
- [21] S. Snyder, S. R. Risbud, and M. Parsa, “Neuromorphic bayesian optimization in Lava,” in *Proc. International Conference on Neuromorphic Systems*, ser. ICONS ’23. New York, NY, USA: ACM, 2023. [Online]. Available: <https://doi.org/10.1145/3589737.3605998>
- [22] S. Snyder, S. Risbud, and M. Parsa, “Asynchronous neuromorphic optimization in Lava,” in *Proc. Great Lakes Symposium on VLSI 2024*, ser. GLSVLSI ’24. New York, NY, USA: ACM, 2024, p. 776–778. [Online]. Available: <https://doi.org/10.1145/3649476.3660383>
- [23] S. Snyder, D. Gobin, V. Clerico, S. R. Risbud, and M. Parsa, “Parallelized multi-agent bayesian optimization in Lava,” in *Proc. International Conference on Neuromorphic Systems*, 2024, pp. 295–298.
- [24] J. Cruz-Duarte, I. Amaya, J. Ortiz-Bayliss, S. Conant-Pablos, H. Terashima-Marín, and Y. Shi, “Hyper-heuristics to customise metaheuristics for continuous optimisation,” *Swarm Evol. Comput.*, vol. 66, p. 100935, 2021.
- [25] J. H. Drake, A. Kheiri, E. Özcan, and E. K. Burke, “Recent advances in selection hyper-heuristics,” *European Journal of Operational Research*, vol. 285, pp. 405–428, 2020, <https://linkinghub.elsevier.com/retrieve/pii/S0377221719306526>. [Online]. Available: <https://doi.org/10.1016/j.ejor.2019.07.073>
- [26] E.-G. Talbi, *Metaheuristics: from design to implementation*. John Wiley & Sons, 2009.
- [27] J. M. Cruz-Duarte, J. C. Ortiz-Bayliss, I. Amaya, Y. Shi, H. Terashima-Marín, and N. Pillay, “Towards a generalised metaheuristic model for continuous optimisation problems,” *Mathematics*, vol. 8, pp. 1–23, 11 2020. [Online]. Available: <https://www.mdpi.com/2227-7390/8/11/2046>
- [28] A. W. Mohamed, A. A. Hadi, and A. K. Mohamed, “Differential evolution mutations: Taxonomy, comparison and convergence analysis,” *IEEE Access*, vol. 9, pp. 68 629–68 662, 2021.
- [29] K. Yamazaki, V.-K. Vo-Ho, D. Bulsara, and N. Le, “Spiking neural networks and their applications: A review,” *Brain Sciences*, vol. 12, no. 7, p. 863, 2022.
- [30] C. D. Schuman, S. R. Kulkarni, M. Parsa, J. P. Mitchell, P. Date, and B. Kay, “Opportunities for neuromorphic computing algorithms and applications,” *Nature Computational Science*, vol. 2, no. 1, p. 10–19, 2022.
- [31] E. M. Izhikevich, “Simple model of spiking neurons,” *IEEE Transactions on Neural Networks*, vol. 14, no. 6, p. 1569, 2003.
- [32] H. S. Steven, *Nonlinear dynamics and chaos: with applications to physics, biology, chemistry, and engineering*. CHAPMAN & HALL CRC, 2024.
- [33] N. Aslimani, E.-G. Talbi, and R. Ellaia, “Tornado: An Autonomous Chaotic Algorithm for Large Scale Global Optimization,” Mar. 2020, working paper or preprint. [Online]. Available: <https://inria.hal.science/hal-02499326>
- [34] Z. Liu, F. Han, and Q. Wang, “A review of computational models for gamma oscillation dynamics: from spiking neurons to neural masses,” *Nonlinear Dynamics*, vol. 108, no. 3, p. 1849–1866, 2022.
- [35] A. Henkes, J. K. Eshraghian, and H. Wessels, “Spiking neural networks for nonlinear regression,” *Royal Society Open Science*, vol. 11, no. 5, p. 231606, 2024.
- [36] J. Kossaifi, A. Khanna, Z. Lipton, T. Furlanello, and A. Anandkumar, “Tensor Contraction Layers for Parsimonious Deep Nets,” *2017 IEEE Conference on Computer Vision and Pattern Recognition Workshops (CVPRW)*, pp. 1940–1946, 2017.
- [37] J. M. Cruz-Duarte and E.-G. Talbi, “Neurooptimisation: The spiking way to evolve - experiment codes and dataset,” Jul. 2025. [Online]. Available: <https://doi.org/10.5281/zenodo.15858610>
- [38] S. Finck, N. Hansen, R. Ros, and A. Auger, “Real-parameter black-box optimization benchmarking 2009: Noiseless functions definitions,” INRIA, Tech. Rep. RR-6829, 2009, updated version as of Feb. 2019. [Online]. Available: <https://inria.hal.science/inria-00362633v2>
- [39] J. de Nobel, F. Ye, D. Vermetten, H. Wang, C. Doerr, and T. Bäck, “IOHexperimenter: Benchmarking Platform for Iterative Optimization Heuristics,” *arXiv*, Nov. 2021. [Online]. Available: <https://arxiv.org/abs/2111.04077>
- [40] A. Auger and R. Ros, “Benchmarking the pure random search on the bbob-2009 testbed,” in *Proc. 11th Annual Conference Companion on Genetic and Evolutionary Computation Conference: Late Breaking Papers*, 2009, pp. 2479–2484.
- [41] M. Davies, N. Srinivasa, T.-H. Lin, G. Chinya, Y. Cao, S. H. Choday, G. Dimou, P. Joshi, N. Imam, S. Jain, Y. Liao, C.-K. Lin, A. Lines, R. Liu, D. Mathaikutty, S. McCoy, A. Paul, J. Tse, G. Venkataramanan, Y.-H. Weng, A. Wild, Y. Yang, and H. Wang, “Loihi: A neuromorphic manycore processor with on-chip learning,” *IEEE Micro*, vol. 38, no. 1, p. 82–99, 2018.